47th AIAA Aerospace Sciences Meeting Including The New Horizons Forum and Aerospace Exposition
5 - 8 January 2009, Orlando, Florida
AIAA 2009-1138

High-Order Shock-Fitting and front-tracking Methods for Numerical Simulation of Shock-Disturbance Interactions

Pradeep S. Rawat[1] and Xiaolin Zhong[2]
University of California, Los Angeles, CA, 90095

High-order methods that can resolve interactions of flow-disturbances with shock waves are critical for reliable numerical simulation of strong-shock and turbulence interaction problems. Such problems are not well understood due to limitations of numerical methods. Most of the popular shock-capturing methods are inherently dissipative and may incur numerical oscillations near the shock. Present paper is continuation of our previous work [1] on development and implementation of new algorithms based on shock-fitting and front-tracking methodology which can solve the flow with high-order accuracy near as well as away from the shocks. The shock-fitting algorithm avoids dissipation and possible numerical oscillations incurred in shock-capturing methods by treating shocks sharply. We explore two ways for shock-fitting: conventional moving grid set-up and a new fixed grid set-up with front tracking. In conventional shock-fitting method, a moving grid is fitted to the shock while in the newly developed fixed grid set-up shock is tracked using Lagrangian points and is free to move across underlying fixed grid. High order front-tracking method gives satisfactory results for 2-D shock disturbance interaction problem. We also studied various methods to find shock velocity. It was found that conventional method of advancing the shock using characteristics based shock-acceleration relation gives more accurate results than other methods considered. Shock-turbulence interaction problems may produce nonlinearities like secondary shocks in the post-shock flow. Hence, we have combined our shock-fitting methodology with shock-capturing methods. Convergence analysis was carried out for combined shock-fitting and WENO methods for an unsteady shock disturbance problem and expected fifth order accuracy was achieved. It was found that, where applicable, shock-fitting algorithm provides superior results to those obtained from purely shock-capturing schemes.

NOMENCLATURE

c= local speed of sound
e= total energy of fluid
M= Mach number
Pr = Prandtl number
$\mathbf{q}$= heat flux vector
T= temperature
T_∞= sonic temperature
U_∞ = sonic velocity at lab conditions
x,y,z= Cartesian coordinates
γ = ratio of specific heats
=
τ = viscous stress tensor
C_v = constant volume specific heat
J= Jacobian of grid transformation
p= pressure
P_0= stagnation pressure of inlet flow.
t = time
T_r= reference temperature
T_o= stagnation temperature
u,v,w = Cartesian velocity components
ρ= density of fluid
μ= dynamic viscosity

[1]Graduate Student, Mechanical and Aerospace Engineering Deptt. pradeep@seas.ucla.edu, Student Member, AIAA
[2]Professor, Mechanical and Aerospace Engineering Department, Associate Fellow, AIAA.

1 INTRODUCTION

Many important scientific and engineering applications involve complex interactions between turbulent flows and strong shocks. Such interactions are part of a number of explosive processes such as volcanic eruptions, detonations, shock wave lithotripsy to break up kidney stones, supernova explosion, as well as the implosion of a cryogenic fuel capsule for inertial confinement fusion (ICF). Numerical simulation of such complex problems warrants very high-order numerical methods. However, popular shock-capturing schemes are not very accurate in this regard as they use dissipation near the shock. Moreover, spurious numerical oscillations have also been observed when solving strong-shock and flow interaction problems with shock-capturing schemes [2]. In the present study, we investigate shock-fitting algorithms for shock and disturbance interaction studies. Problem of interaction of normal shock and disturbances is fundamental for better understanding of the aforementioned complex phenomena. To this end, shock-fitting methods developed in current effort can be very useful to find high-order solutions of some simple shock and turbulence interaction problems such as shown in Fig. 1. Various researchers have considered such shock and disturbance/turbulence interaction problems in past. A brief summary is presented in ensuing sections for previous works in the field, followed by the scope of current study.

1.1 Theoretical Studies

Theoretical studies in this field have been attempted mostly through linear interaction analysis (LIA) where small perturbations in flow are considered. Kovasznay [3] showed that for weak fluctuations of density, pressure, and entropy, the turbulent fluctuations about mean uniform flow can be decomposed into the vorticity, acoustic, and entropy modes. It was shown that for first order approximation, each of these modes evolve independently in the inviscid limit for mean uniform flow. However, in second order approximation of fluctuations, interaction of these modes is possible and one mode can be generated from interaction of other two modes [4].

Ribner [5-7] and Moore [8] were among the earliest workers to consider theoretically the passing of a turbulent field through a shock wave. Ribner [5] analyzed interaction of a plane sinusoidal disturbance in velocity (shear wave) passing through a shock as a boundary value problem. In his analysis the shock was kept steady by solving the equations in a moving reference frame. It was found that initial shear wave is amplified and refracted by the shock due to the changes in thermodynamic properties and therefore emerges at a different angle from the incident. He later generalized this result from single wave to obtain shock-interaction effects of a completely turbulent velocity field [6] and obtained significant turbulent amplification due to shock turbulence interaction. The results were further extended [7] to provide the flux of acoustic energy emanating from unit area on the downstream of the shock. Moore [8] performed unsteady analysis of interaction of obliquely traveling weak plane disturbances of arbitrary profile with a plane normal shock. Unlike Ribner's analysis, unsteady shock was considered for linear analysis the interaction of sound and vorticity waves with an unsteady shock. It was found that amplification of disturbances depends on impingement angle and Mach number of the shock. Kerrebrock [9] considered modifications of random small fluctuations of pressure, entropy and vorticity in passing through shock or flame. It was found that all modes of disturbances are generated in the downstream flow if any of the modes is present in the upstream flow. McKenzie and Westphal [10] derived formulas for amplification and Snell's Laws for refraction and reflection of acoustic, vorticity and entropy waves interacting with shock and applied the results

to the amplification of small disturbances in the solar wind on a passage through the bow shock of earth. More recent theoretical studies of shock and turbulence interaction are by Goldstein [11], Lee et al. [12-14], Mahesh et al. [15-17] and Fabre et al. [18, 19]. It was found in these studies that different components of the turbulent kinetic energy, as well as root mean square values of the fluctuating pressure, temperature and density are amplified across the shocks. Despite several assumptions, Linear Interaction Analysis (LIA) provides accurate description of the essential characteristics of the interaction.

1.2 Numerical Studies

Since the early 80s, various attempts have been made towards numerical simulation of shock and disturbance/turbulence interaction. Initial efforts in this regard considered interaction of shock with simple waves. In 1981, Pao and Salas [20] fitted the shock at inflow boundary and solved Euler equation with finite difference discretization for study of shock/vortex interaction. Shock fitting computations with pseudo-spectral (Zang et. al [21]) and spectral techniques (Hussaini et al [22, 23]) were later used to treat the problems in which a single vortex, a vortex sheet, an entropy spot or acoustic wave interacts with the shock. The results obtained from these numerical efforts confirmed the linear theory in the regime of weak shocks. With the advent of essentially non-oscillatory (ENO) and related schemes, shock-capturing methods gained popularity for simulations of compressible flows. A number of new schemes for compressible flows has since been tested for interaction of shock with small disturbances against the results obtained from linear theory [23-25]. Although limited to low Mach numbers, these studies mostly confirm the LIA results.

The numerical studies of fully turbulent field interacting with shocks are more recent. For the simulation of the turbulent field DNS methods and large eddy simulations (LES) have been used. However these different types of methods give different results when interaction with shock is considered [26]. Most of the recent direct numerical simulation (DNS) studies have been on various aspects of interaction of a normal shock with freestream turbulence for relatively weak shock of small Mach numbers. For example, Mahesh et al. [15, 17] did extensive direct numerical simulation (DNS) study of the interaction of a normal shock with an isotropic turbulence. The mean shock Mach numbers were in the range of 1.29 to 1.8. They found that the upstream correlation between the vorticity and entropy fluctuations has strong influence on the evolution of the turbulence across the shock. They also used linear analysis to analyze the simulation results. Other shock/turbulence interaction studies have been conducted by the same group of workers [12, 13]. Lee et al. [13] investigated the effect of Mach number on isotropic vertical turbulence interacting with a shock wave. The range of Mach numbers was in the range from 1.5 to 3.0. A shock-capturing scheme was developed to accurately simulate the unsteady interaction of turbulence with shock waves. It was found that turbulence kinetic energy is amplified across the shock wave, and this amplification tends to saturate beyond Mach 3. Hannapel et al. [27] computed interaction of a Mach 2 shock with a third order in space shock-capturing scheme based on the essentially non-oscillatory ENO algorithm of Harten together with an approximate Riemann solver. Jamme et al. [28] carried out a Direct Numerical Simulation (DNS) to study the interaction between normal shock waves of moderate strength (Mach 1.2 and Mach 1.5) and isotropic turbulence. Adams and Shariff [29, 30] proposed a class of upwind-biased finite-difference schemes with a compact stencil for shock/turbulence interaction simulation. They used this nonconservative upwind scheme in smooth region while a shock-capturing ENO scheme was turned on around discontinuities. This idea of hybrid

formulation was improved by Pirozzoli [31] who used similar hybrid formulation for a compact weighted essentially non-oscillatory (WENO) scheme with conservative formulation for simulation of shock turbulence interaction. Ducros et al. [32] developed larger-eddy simulation(LES) on the shock/turbulence interaction by using a second-order finite volume scheme. The method was then used to simulate the interaction of a Mach 1.2 shock with homogeneous turbulence.

Yee et al. [33] proposed characteristic-type filters, which add the dissipative part of traditional shock capture schemes to non-dissipative central based schemes in order to damp out numerical instabilities. Due to this feature, characteristic filters are very suitable to incorporate into existing LES codes based on high-order methods, and they allow the codes to have shock capturing capability. This scheme was used by Sjogreen and Yee [34] for shock disturbance interaction. Recently, Cook and Cabot [35] developed artificial viscosity formulations for shock-turbulence simulations. It functions as an effective subgrid-scale model for both high and low Mach number flows. The model employs a bulk viscosity for treating shocks and a shear viscosity for treating turbulence and has been used for the basic shock disturbance interaction.

It is observed that most of the studies in field of shock-turbulence interaction have considered weak shocks only. Recently, more efforts have been directed towards investigating turbulent flows with stronger shocks which is relevant for a lot of high-speed compressible flows. Main issue with shock-capturing schemes is spurious numerical oscillations around the shock and loss of accuracy with dissipation needed to suppress these oscillations. Moreover, with stronger shocks, shock-thickness reduces which requires a finer resolution with shock-capturing schemes. Shock-fitting method offers a good alternative for strong shocks with simple geometries as shock is considered a sharp discontinuity. As mentioned before, one of the earliest numerical methods considered for shock-disturbance interactions were based on shock-fitting methodology. Shock-fitting methods have also been very successful for high-order simulations for freestream disturbances interacting with shock on blunt body [36-39] . Recently, Sesterhenn et al. [40] revisited shock-fitting schemes and applied them for solving Navier-Stokes equations in non-conservative form for problem of interaction of Mach 3 shock with isotropic turbulence with encouraging results. Shock-fitting considers the shock as a sharp discontinuity and is well equipped to consider even stronger shocks without any need for grid refinements. Shock-fitting algorithms can be even more useful in front-tracking methods where shock can move across the fixed grids avoid. Shock-fitting methods, however, can be really cumbersome for three dimensional problems and complex phenomena where shock merging and breaking takes place which is handled well by shock-capturing schemes. Moreover, even when we have a well defined strong shock that should be fitted, there could be nonlinear features like secondary shocks present in the flow which require shock-capturing schemes. Thus, there are there is need to use shock-fitting and shock-capturing schemes in a hybrid setting.

1.3 Motivation and Scope of Current Study

A study of the literature in the field of shock interactions with disturbances and turbulence shows that these complex configurations are part of a number of important phenomena including supernova explosions and inertial confinement fusion. However, the current scientific understanding of shock-turbulence interactions in complex configurations and the ability to reliably predict these strongly nonlinear flows remains limited. Most of the popular methods for solving compressible flow involve shock-capturing algorithms for treatment of shock. However, it has been observed that even high-order shock capturing methods give low

accuracy at the shock [41] and might lead to spurious oscillations [2]. Many shock capturing methods introduce some dissipation to avoid spurious oscillations which, however, is not accurate enough for simulation of turbulent flow. On the other hand, conventional high-order methods generally used for DNS studies have numerical problems due to strong gradients around shock. Due to such problems, DNS of shock and isotropic turbulence interaction has not been possible for stronger than Mach 3 shocks due to limitations of computational resources for the used shock capturing algorithms.

Current work is continuation of our efforts presented in Ref. [1]. Here, underlying idea is to develop and use shock-fitting and interface fitting algorithms along with high order schemes to gain knowledge about nonlinear phenomena involving interaction of strong shocks and turbulent flows. Shock or interface fitting algorithms treat the interface sharply without any dissipation hence they are compatible with low dissipation schemes used for DNS of turbulent flow. Shock/interface fitting methods are ideally suited for the cases where there is a clearly demarcated interface which is indeed the case for the problem of turbulent flow incoming to a strong shock as shown in Fig. 1. In our previous work [1], we considered some simple canonical problems and established the high-order accuracy of the shock-fitting methods for such problems. All these factors provide ample motivation to further enhance and develop shock-fitting algorithms for solving shock-turbulence interaction problems.

Conventionally, shock is treated as boundary in shock-fitting methods and grids follow the shock during the computations. This, however, might not be feasible if shape of the shock becomes complex or there are large movements in shock. For such situations, it is more useful to extend high-order shock-fitting idea to use with fixed grids where shock moves independent of grids. Hence, an aim of current study is to develop new methods and algorithms to use idea of shock-fitting on fixed grids with the help of front-tracking method. We have developed a 2-D algorithm based on front-tracking where we use Lagrangian type marker points to track the shock-front. Shock velocity is obtained from a shock acceleration equation following conventional shock-fitting method used by Zhong [42]. Method is described in section 4 while results for two-dimensional shock-disturbance problems are presented in section 5.

We also realize that there can be several different ways to determine shock-movement. We explore some of these methods and assess the quality of results obtained for shock-disturbance interaction problems. To this end, we carry out a convergence analysis with various methods for finding shock-velocity which is presented in section 6.

Although, high order central difference schemes with shock-fitting algorithm are highly accurate, they are limited in scope. For the shock and isotropic turbulence interaction problems which we intend to solve, the main shock generally remains well defined which can be fitted but weak discontinuities like secondary shocks are generated in the post shock-flow. Hence, to take advantage of both shock-fitting and shock-capturing methods, we have combined them and convergence study for unsteady shock-disturbance interaction problem is carried out in section 7.

Thus main thrust of current study includes (a) studying accuracy and results of conventional shock-fitting algorithm with high-order central scheme as well as shock-capturing schemes for some canonical problems (b) implementing shock-fitting algorithm with a fixed grid solver and (c) assess various methods for finding shock-velocity to use in shock-fitting algorithms.

In remaining part of this paper we briefly present the governing equations and numerical method followed by solutions for the cases of 1-D and 2-D disturbances interacting with shock.

2 GOVERNING EQUATIONS

The governing equations are compressible Navier-Stokes equations which are given as follows:

$$\frac{\partial \rho}{\partial t} + \nabla.(\rho \mathbf{u}) = 0 \tag{1}$$

$$\rho\left(\frac{\partial \mathbf{u}}{\partial t} + \mathbf{u}\cdot\nabla\mathbf{u}\right) = -\nabla p + \nabla\cdot\bar{\bar{\tau}} \tag{2}$$

$$\frac{\partial e}{\partial t} + \nabla\cdot(e\mathbf{u}) = -\nabla\cdot(p\mathbf{u}) + \nabla\cdot(\mathbf{u}\cdot\bar{\bar{\tau}}) - \nabla\cdot\mathbf{q} \tag{3}$$

where $e = \frac{p}{(\gamma-1)} + \frac{1}{2}\rho U^2$, is the internal energy plus the kinetic energy of the fluid. The viscous stress and the heat flux are given by the usual constitutive equations in Newtonian fluid as follows

$$\tau_{ij} = \mu\left(\frac{\partial u_i}{\partial x_j} + \frac{\partial u_j}{\partial x_i}\right) - \frac{2}{3}\mu\frac{\partial u_k}{\partial x_k}\delta_{ij} \tag{4}$$

$$q_i = -k\frac{\partial T}{\partial x_i} \tag{5}$$

where μ is the viscosity coefficient determined by the Sutherland law,

$$\mu = \mu_r\left(\frac{T}{T_r}\right)^{\frac{3}{2}}\frac{T_r + T_s}{T + T_s} \tag{6}$$

where T_r = 288K, T_s = 110K, and μ_r = 0.17894 × 10^{-4} kg/m/s for air. The thermal conductivity k is computed from the Prandtl number, which is assumed constant and it takes the value of 0.72 in this paper.

3 NUMERICAL METHOD: CONVENTIONAL HIGH-ORDER SHOCK-FITTING

For conventional moving-grid shock-fitting approach, shock forms a boundary of the computational domain and fifth-order shock-fitting method of Zhong [42] is used for solving the flow between shock and exit boundary (Fig. 1). The flow variables just behind the shock are determined by Rankine-Hugoniot relations across the main shock and a characteristic compatibility relation from behind the shock. The velocity and location of the shock are solved as part of the solutions and grid is modified to follow motions of the shock. In the interior,

solution of conservative compressible Navier-Stokes equations is carried out using the numerical method described in this section.

In numerical simulation, the compressible Navier-Stokes equations (2) to (4) are written in the following conservative form,

$$\frac{\partial U}{\partial t}+\frac{\partial E}{\partial x}+\frac{\partial F}{\partial y}+\frac{\partial G}{\partial z}+\frac{\partial E_v}{\partial x}+\frac{\partial F_v}{\partial y}+\frac{\partial G_v}{\partial z}=0 \tag{7}$$

where U is the solution vector given by

$$U=\{\rho,\rho u,\rho v,\rho w,e\} \tag{8}$$

E, F, G are the inviscid flux terms, and E_v, F_v, G_v are the viscous terms. They are written as follows

$$E=\begin{Bmatrix}\rho u\\ \rho u^2+p\\ \rho uv\\ \rho uw\\ (e+p)u\end{Bmatrix} \tag{9}$$

$$F=\begin{Bmatrix}\rho v\\ \rho vu\\ \rho v^2+p\\ \rho vw\\ (e+p)v\end{Bmatrix} \tag{10}$$

$$G=\begin{Bmatrix}\rho w\\ \rho wu\\ \rho wv\\ \rho w^2+p\\ (e+p)w\end{Bmatrix} \tag{11}$$

$$E_v=\begin{Bmatrix}0\\ \tau_{xx}\\ \tau_{yx}\\ \tau_{zx}\\ u\tau_{xx}+v\tau_{yx}+w\tau_{zx}-q_x\end{Bmatrix} \tag{12}$$

$$F_v = \begin{Bmatrix} 0 \\ \tau_{xy} \\ \tau_{yy} \\ \tau_{zy} \\ u\tau_{xy} + v\tau_{yy} + w\tau_{zy} - q_y \end{Bmatrix} \tag{13}$$

$$G_v = \begin{Bmatrix} 0 \\ \tau_{xz} \\ \tau_{yz} \\ \tau_{zz} \\ u\tau_{xz} + v\tau_{yz} + w\tau_{zz} - q_z \end{Bmatrix} \tag{14}$$

In the conservative equation (7), the inviscid fluxes and the viscous fluxes have the same forms as those of the Navier-Stokes equations. Before discretizing the governing equations by a finite difference method, equation (7) in the physical domain is transformed to the shock and boundary fitted computational domain by the following transformation relations,

$$\begin{cases} \xi = \xi(x, y, z) \\ \eta = \eta(x, y, z) \\ \varsigma = \varsigma(x, y, z) \\ \tau = t \end{cases} \Leftrightarrow \begin{cases} x = x(\xi, \eta, \varsigma, \tau) \\ y = y(\xi, \eta, \varsigma, \tau) \\ z = z(\xi, \eta, \varsigma, \tau) \\ t = \tau \end{cases} \tag{15}$$

and the transformed governing equation in the computational domain is expressed as follows

$$\frac{1}{J}\frac{\partial U}{\partial \tau} + \frac{\partial E'}{\partial \xi} + \frac{\partial F'}{\partial \eta} + \frac{\partial G'}{\partial \varsigma} + \frac{\partial E'_v}{\partial \xi} + \frac{\partial F'_v}{\partial \eta} + \frac{\partial G'_v}{\partial \varsigma} + U\frac{\partial\left(\frac{1}{J}\right)}{\partial \tau} = 0 \tag{16}$$

3.1 High Order Upwind Finite difference Scheme

Shock-fitting methodology can be applied with any scheme. In current study we have used a 5th order upwind scheme and a 5th order WENO scheme for this purpose. An explicit finite difference scheme from Ref [42] is used for spatial discretization of the governing equation (16). The inviscid flux terms are discretized by a fifth-order upwind scheme, and the viscous flux terms are discretized by a sixth-order central scheme. For the inviscid flux vectors, the flux Jacobians contain both positive and negative eigenvalues. A simple local Lax-Friedrichs scheme is used to split vectors into negative and positive wave fields. For example, the flux term F′ in Eq (16) can be split into two terms of pure positive and negative eigenvalues as follows

$$F' = F'_+ + F'_- \tag{17}$$

where $F'_+ = \frac{1}{2}\left(F' + \lambda U\right)$ and $F'_+ = \frac{1}{2}\left(F' - \lambda U\right)$ and λ is chosen to be larger than the local maximum eigenvalue of F′.

$$\lambda = \frac{|\nabla \eta|}{J}\left(\sqrt{(\varepsilon c)^2 + u'^2} + c\right) \tag{18}$$

where

$$u' = \frac{\eta_x u + \eta_y v + \eta_z w + \eta_t}{|\nabla \eta|} \tag{19}$$

The parameter ε is a small positive constant added to adjust the smoothness of the splitting. The fluxes F'_+ and F'_- contain only positive and negative eigenvalues respectively. Therefore, in the spatial discretization of Eq. (7), the derivative of the flux F is split into two terms

$$\frac{\partial F'}{\partial \eta} = \frac{\partial F'_+}{\partial \eta} + \frac{\partial F'_-}{\partial \eta} \tag{20}$$

where the first term on the right hand side is discretized by the upwind scheme and the second term by the downwind scheme.

The fifth-order explicit scheme utilizes a 7-point stencil and has an adjustable parameter α as follows

$$u'_i = \frac{1}{hb_i}\sum_{k=-3}^{3} a_{i+k}u_{i+k} - \frac{\alpha}{6!b_i}h^5\left(\frac{\partial^6 u}{\partial x^6}\right)_i + \ldots \tag{21}$$

where $a_{i\pm3} = \pm 1 + \frac{1}{12}\alpha$ $\alpha_{i\pm3} = \pm 1 + \frac{1}{12}\alpha,\ \alpha_{i\pm2} = \mp 9 - \frac{1}{2}\alpha,\ \alpha_{i\pm1} = \pm 45 + \frac{5}{4}\alpha,\ \alpha_i = -\frac{5}{3}\alpha$ and $b_i = 60$. The scheme is upwind when α < 0 and downwind when α > 0. It becomes a 6-order central scheme when α = 0 which is used for discretizing viscous terms.

3.2 Fifth Order WENO Schemes

In the typical shock-turbulence interaction problem, as described in Fig. 1, the flow behind the main shock may encounter formation of weak secondary shocks. Hence, even as the main shock is fitted, a shock-capturing scheme is needed to solve the flow behind the fitted shock. We have combined the shock-fitting algorithm with a couple of 5th order weighted essentially non-oscillatory (WENO) schemes. First WENO scheme is based on Jiang and Shu's [43] formulations and, following the literature, will be referred in this paper as WENO5 scheme. Henrick et al [44] suggested an improvement over WENO5 to get more accurate solutions in the smooth region. This scheme will be referred in this study as WENO5M.

In WENO5 scheme, spatial derivative of any scalar function f is approximated as follows:

$$\left.\frac{\partial f(u)}{\partial x}\right|_{x=x_j} \approx \frac{\hat{f}_{j+1/2} - \hat{f}_{j-1/2}}{\Delta x} \tag{22}$$

Where $\hat{f}_{j+1/2}$ is approximation to the numerical flux function which is constructed as weighted sum of fluxes from three different three point stencils as:

$$\hat{f}_{j+1/2} = \omega_1 \hat{f}^{(1)}_{j+1/2} + \omega_2 \hat{f}^{(2)}_{j+1/2} + \omega_3 \hat{f}^{(3)}_{j+1/2} \tag{23}$$

Where,

$$\begin{aligned}
\hat{f}^{(1)}_{j+1/2} &= \frac{1}{3} f_{j-2} - \frac{7}{6} f_{j-1} + \frac{11}{6} f_j \\
\hat{f}^{(2)}_{j+1/2} &= -\frac{1}{6} f_{j-1} + \frac{5}{6} f_j + \frac{1}{3} f_{j+1} \\
\hat{f}^{(3)}_{j+1/2} &= \frac{1}{3} f_j + \frac{5}{6} f_{j+1} - \frac{1}{6} f_{j+2}
\end{aligned} \tag{24}$$

and ω_i are nonlinear weights given by

$$\omega_i = \frac{\sigma_i}{\sum_{k=1}^{3} \sigma_k}, \quad where \quad \sigma_i = \frac{\gamma_i}{\left(\varepsilon^* + \beta_k\right)^2} \tag{25}$$

Here, γ_i represent the ideal weights, which give 5th order scheme with Eq.(23) and are given as

$$\gamma_1 = \frac{1}{10}, \quad \gamma_2 = \frac{3}{5}, \quad \gamma_3 = \frac{3}{10} \tag{26}$$

and the indicators of smoothness, β_k are given by:

$$\begin{aligned}
\beta_1 &= \frac{13}{12}\left(f_{j-2} - 2f_{j-1} + f_j\right)^2 + \frac{1}{4}\left(f_{j-2} - 4f_{j-1} + 3f_j\right)^2 \\
\beta_2 &= \frac{13}{12}\left(f_{j-1} - 2f_j + f_{j+1}\right)^2 + \frac{1}{4}\left(f_{j-1} - f_{j+1}\right)^2 \\
\beta_3 &= \frac{13}{12}\left(f_j - 2f_{j+1} + f_{j+2}\right)^2 + \frac{1}{4}\left(3f_j - 4f_{j+1} + 3f_{j+2}\right)^2
\end{aligned} \tag{27}$$

ε^* is a constant used to keep the weights bounded. Equations. (23)-(27) describe WENO5 scheme and generally $\varepsilon^* = 1e-6$ is used to obtain fifth order accuracy in the smooth region while keeping the solution stable near the discontinuities. Henrick et al.[44] suggest that accuracy of the solution can be improved by mapping the weights in Eq. (25) to get the final weights as

$$\bar{\omega}_i = \frac{g_i(\omega_i)}{\sum_{k=1}^{3} g_k(\omega_k)} \tag{28}$$

Where $g_k(\omega)$ is the mapping function given by

$$g_k(\omega) = \frac{\omega\left(\sigma_{k+}\sigma_k^2 - 3\sigma_k\omega + \omega^2\right)}{\sigma_k^2 + \left(1 - 2\sigma_k\right)\omega} \tag{29}$$

So instead of equation (23) the WENO5M scheme uses

$$\hat{f}_{j+1/2} = \bar{\omega}_1 \hat{f}^{(1)}_{j+1/2} + \bar{\omega}_2 \hat{f}^{(2)}_{j+1/2} + \bar{\omega}_3 \hat{f}^{(3)}_{j+1/2} \tag{30}$$

As detailed in Refs [43] and [44], for solution of Euler equations, a simple local Lax-Friedrichs flux splitting is first carried out for flux terms in all directions following Eqs. (17)-(20) to divide the flux vector into negative and positive wave fields. The procedure for finding smoothness indicators β_k and weights ω_i (for WENO5 scheme) or $\bar{\omega}_i$ (for WENO5M schemes) is carried out in local characteristic fields. Thus we first find Roe average [45] of grid point values and based on eigenvectors of Jacobian, transform all the quantities needed for evaluating numerical flux to local characteristic fields. The numerical fluxes in each characteristic field are found by using the scalar procedure described above and then transformed back to original physical space.

Our shock-fitting method [42] uses flux values at the shock points to find the shock-acceleration which in turn is used to advance the shock. The WENO schemes described above need three points either side of any grid point, hence we use one-sided finite difference scheme for the grid points where WENO stencil may cross the shock. Figure 2 shows a schematic of the computational domain highlighting the points where one-sided should be used. Specifically, if the shock lies on the grid line represented as $I = IL$, one-sided finite differencing is used for points with $I = IL - 2, IL$. There are many choices available for one sided finite difference schemes for 3 points close to the boundary, which are considered for convergence study in section 7.

4 NEW FRONT-TRACKING BASED HIGH-ORDER SHOCK-FITTING METHOD

Conventional shock-fitting methodology, as described in previous sections, assumes the shock to be the boundary of the domain and flow is solved on moving grids. However, this approach becomes very difficult to apply for a problem where shock geometry becomes complex or the shock performs large motions. Hence, it is useful to develop a methodology that can implement ideas of shock-fitting algorithm on fixed grids. We have explored a fixed grid shock-fitting method where shock is treated as an interface and can move across the fixed grid points. Thus the method is along the lines of fixed grid Cartesian grid methods like Immersed Boundary Method (IBM)[46] and Immersed Interface Method (IIM) [47] and Ghost-fluid method [48] coupled with methods to track the front (shock)[49]. The methodology is presented here in brief for two dimensional problems.

4.1 Finite Difference Scheme

Similar to the conventional shock-fitting, governing equations are solved in the conservation form of equations and physical domain is transformed to computational domain and flux splitting is performed for application of upwind finite-difference schemes. Thus Eqs. (1) - (20) are still applicable in this formulation except fixed grids are used with a constant Jacobian of grid-transformation. The 5th order upwind method given by (21) can be used on the points where finite-difference stencil does not cross the front. However, special treatment is needed for the "irregular" points where the stencil requires points on both sides of the shock. An example of irregular points on a grid line in X-direction is shown as the highlighted points shown in Fig.3 for 7 point 5th order scheme. Similar irregular grid points can also be found for Y-direction grid line.

To avoid crossing of shock-front by stencils we use one-sided finite differencing on irregular points. Interface point is included in the stencil along with interior points and we use one sided Lagrange interpolation to find derivative of any variable u at point x_j as follows:

$$\left[\frac{\partial u}{\partial x}\right]_{x=x_j} = \sum_{k=-n+1}^{0} l_k'(x_j)u_{i+k} + l_\Gamma'(x_j)u_\Gamma \tag{31}$$

where subscript Γ indicates interface point, x_i is the nearest point to the interface that is taken in the one sided difference stencil and Lagrange coefficients l_k's and l_Γ are given as

$$\begin{aligned} l_k(x) &= \frac{\sum_{p=0,p\neq k}^{-n+1}(x-x_{i+p})}{\sum_{p=0,p\neq k}^{-n+1}(x_{i+k}-x_{i+p})}\left(\frac{(x-x_\Gamma)}{(x_{i+k}-x_\Gamma)}\right) \\ l_\Gamma(x) &= \frac{\sum_{p=0}^{-n+1}(x-x_{i+p})}{\sum_{p=0}^{-n+1}(x_\Gamma-x_{i+p})} \end{aligned} \tag{32}$$

It should be noted that when using one-sided derivatives there might be issues with stability of the method if the stencil has one of the grid points very close to the interface. Hence choice of stencil is based on relative separation of interface point from nearest grid given by

$$\sigma = \frac{|x_i - x_\Gamma|}{|x_i - x_{i+1}|}. \tag{33}$$

A critical value, σ^*, of this relative separation is used to decide the stencil taken for one-sided differencing. Two cases are possible:

(a) $\sigma \geq \sigma^*$: When marker point and interface have reasonable separation (as shown in Fig. 4(a) then include in the stencil, the marker point as well as the closest point and store all the coefficients (as shown in the Fig. 4(a)).

(b) $\sigma < \sigma^*$: When marker point and one of the interface point are too close, we will include the marker point but leave out the closest grid point and include a grid point on other end instead (as shown in Fig. 4(b)). Values at closest grid-points are updated by high-order interpolations from other points of the stencil.

It was found that as we increase σ^*, the code becomes more and more stable. For the results presented in this paper we use $\sigma^* = 1$. One-sided finite differencing is used to avoid finite difference stencils crossing the shock-front. However, if appropriate jump conditions are known at the shock-front, one can use schemes like Immersed interface methods (IIM) that find the finite differences at irregular grid points using regular stencil and correction terms based on jump conditions. Such methods allow flow of information across the shocks and can be more accurate as accurate jump conditions are enforced. Moreover, ad-hoc parameter σ^* would not be needed. Recently, Zhong [47, 50] developed a new immersed interface algorithm that requires jumps only in values of flow variables and their first derivatives while showing arbitrarily high-order accuracy. Since upto first order jump conditions can be derived from physics of the problem, this method is more suitable for high-order computations of real problems than other IIM schemes which need higher order derivatives of flow variables to obtain higher order of accuracy. Such IIM schemes should be considered in future as improvement on one-sided finite differencing scheme.

4.2 Representation of the Front

In our methodology, the shock-front is assumed to be sharp and is represented using Lagrangian marker points. The marker points connect segments of 5th order polynomial curves. For convenience in taking finite differences across the shock front, intersection points of the front with the grid lines are chosen as marker points. Figure 5 shows typical marker points (S_i, S_{i+1} etc.) for a shock-front moving across a two-dimensional grid. These marker points are stored in a sequenced list. The order in list indicates the immediate neighboring markers of a marker as shown in the Fig. 5. The notation used here is such that as we move along the markers by incrementing in this sequenced list, the low pressure side of the shock should be on the left. With each marker point, information regarding geometry of the front, flow properties corresponding to the marker points and relation of marker point with the fixed grid is also needed to be saved. Some important points about treatment of front are as follows:

Shock geometry:

With each marker point, coordinates of the marker points are computed and saved. A critical part of information regarding shock-geometry for shock-fitting method is shock shape, specifically, shock normal and shock tangents which are obtained using the coordinates. We use following parametric representation for the marker points to obtain shock normal and shock tangents:

$$\begin{aligned} x &= x(s) \\ y &= y(s) \end{aligned} \tag{34}$$

where s represents the arc-length on the interface. Arc-length is chosen as the parameter to represent the surface since value of arc-length monotonically increases along the surface and each value of arc-length coordinate correspond to a unique point on the interface. Moreover, arc-

length represents the value of body-fitted coordinate in the tangential direction which can be readily used to obtain tangential derivatives of various flow variables where needed. Using arc-length as parameter we use following definition for normal and tangent in 2-D.

$$n_x = \frac{\frac{\partial y}{\partial s}}{\left[\left(\frac{\partial x}{\partial s}\right)^2 + \left(\frac{\partial y}{\partial s}\right)^2\right]^{\frac{1}{2}}}, \quad n_y = \frac{-\frac{\partial x}{\partial s}}{\left[\left(\frac{\partial x}{\partial s}\right)^2 + \left(\frac{\partial y}{\partial s}\right)^2\right]^{\frac{1}{2}}},$$
$$\tau_{1x} = \frac{\frac{\partial x}{\partial s}}{\left[\left(\frac{\partial x}{\partial s}\right)^2 + \left(\frac{\partial y}{\partial s}\right)^2\right]^{\frac{1}{2}}}, \quad \tau_{1y} = \frac{\frac{\partial y}{\partial s}}{\left[\left(\frac{\partial x}{\partial s}\right)^2 + \left(\frac{\partial y}{\partial s}\right)^2\right]^{\frac{1}{2}}}, \tag{35}$$

This way of taking normal ensures that normal goes from high-pressure side towards low-pressure side. Thus using the direction of normal at any marker point we are able to determine orientation of high pressure side and low pressure side with respect to the given marker point. It should be noted, however, that arc-length is not directly known from the coordinate points. To obtain arclength and values of normal and tangents, we use an iterative procedure, where initial value of arclength is approximated as summed distance between the marker points. Using this approximate value as parameter we find coefficients of 5th order polynomial segments and corresponding values of corrected arc length. The process is repeated till the values of arc-length are sufficiently converged.

Communication between the front and the grid

It can be observed that for two dimensional grid, there are two types of marker points: those at the intersection with Y=const line (ξ-grid line) and those at the intersection with X=const (η -grid line). Since each marker point is an intersection point, relation between grid and marker point is established by storing type of intersection point (intersecting with ξ-line or η -line) and indices for intersecting grid-line for each marker point. Indices of irregular grid points associated with marker points are also stored with each marker for efficient implementation of one-sided finite difference. Moreover, at each grid point, an indicator value, ϕ, is saved to associate the grid point with high pressure or low pressure side as appropriate. There could also be some grid points lying between interface points where one-sided differencing may not be applied as enough points are not available. Such points are "skipped" while taking fluxes and a unique value of indicator function is assigned to mark such points. Following value of indicator function is defined at every grid-point.

$\phi = 1$ for normal points on the low pressure side
$\phi = -1$ for normal points on the high pressure side
$\phi = 2$ for skipped points on the low pressure side on a ξ-grid line
$\phi = -2$ for skipped points on the high pressure side on a ξ-grid line

$\phi = 3$ for skipped points on the low pressure side on an η-grid line
$\phi = -3$ for skipped points on the high pressure side on an η-grid line
$\phi = \pm 4$ for points which do not have enough points in both directions.

For each marker point, indicator values at neighboring grid points are checked to see if there are any grid-points with $|\phi| > 1$. Since flux values can not be computed at such grid points, these points are updated using interpolations. For $|\phi| = 2$ points, we choose points along corresponding η-grid line and interpolate while ξ-grid line is use for interpolation at grid points with $|\phi| = 3$. Figure 6 shows an example of $\phi = -2$ points and the points used for interpolations at such points. Other cases can be explained similarly.

Shock Velocity based on Shock-acceleration.

We use standard shock-fitting technique of finding the shock acceleration using Rankine-Hugoniot jump conditions at the shock coupled with characteristic information from high-pressure side of the flow. In the conventional shock-fitting method, the shock is represented as a moving grid-surface of the computational domain. Hence, shock velocity is related to the grid velocity and metrics of the grid transformation. Since the shock is represented by grid points, values of flow variables are readily available for use in finding shock-acceleration at the shock points. Method to find the shock acceleration in conventional shock-fitting is described in detail in Ref [42]. The conventional shock-fitting method for finding shock-velocity can be carried over to the Front-tracking method on a fixed grid by defining an imaginary grid associated with each marker point. Figure 7 shows a schematic of the real shock-front on a fixed grid (Fig. 7(a)) and associated imaginary grid-set used to find the shock-acceleration at i^{th} marker point (Fig. 7(b)). The marker point P_i represents a grid point in this imaginary grid-set and there can be a number of choices for other grid points. We choose η^* - grid line passing through P_i to be parallel to $\vec{\mathbf{n}}$ of shock-front so that shock-acceleration is obtained in the normal direction. The base ξ^*-grid surface for this imaginary grid-set is chosen to be in parallel direction to tangent plane of the shock-front at P_i. Having established directions for this imaginary grid, we choose to define coordinates in the computational domain at particular moment of time by orthogonal transformation from physical space, i.e.

$$\begin{bmatrix} \xi^* - \xi_s^* \\ \eta^* - \eta_s^* \\ \zeta^* - \zeta_s^* \end{bmatrix} = \begin{bmatrix} \tau_{1x} & \tau_{1y} & \tau_{1z} \\ n_x & n_y & n_z \\ \tau_{2x} & \tau_{2y} & \tau_{2z} \end{bmatrix} \begin{bmatrix} x - x_s \\ y - y_s \\ z - z_s \end{bmatrix} \tag{36}$$

Here, $\vec{\mathbf{n}}$ represents normal at the given point P_i, $\overrightarrow{\boldsymbol{\tau}_1}$ and $\overrightarrow{\boldsymbol{\tau}_2}$ are tangent vectors. τ_{1x} represents angle of vector $\overrightarrow{\boldsymbol{\tau}_1}$ with x-axis and similarly other terms in the matrix are direction cosines of vectors $\overrightarrow{\boldsymbol{\tau}_1}$, $\vec{\mathbf{n}}$ and $\overrightarrow{\boldsymbol{\tau}_2}$. $\left(\xi_s^*, \eta_s^*, \zeta_s^*\right)$ and $\left(x_s, y_s, z_s\right)$ represent coordinates of shock-point P_i in computational and physical domain respectively.

Once appropriate relation is established between real fixed grid and imaginary set of moving grids, one can directly use the methodology of conventional shock-fitting. Following the relations given by Zhong [42] and noting that for the coordinate transformation given by (36) we have $\left|\nabla \eta^*\right|$=1 and Jacobian of transformation at the given point of time J^* = 1, one obtains following relation for shock acceleration

$$\frac{\partial v_n}{\partial t} = \frac{1}{\left[\mathrm{I_N}\cdot\left(\mathrm{U_s}\text{-}\mathrm{U_0}\right)\right]}\left[\left(u_n - v_n + c\right)\mathrm{I_N}\cdot\left(\frac{\partial \mathrm{U}}{\partial \tau^*}\right)_s + \mathrm{I_N}\cdot\left(\mathbf{F_s}\text{-}\mathbf{F_0}\right)\cdot\frac{\partial \mathbf{a}}{\partial \tau^*} - \mathrm{I_N}\cdot\left(\frac{\partial \mathbf{F_0}}{\partial \tau^*}\cdot\mathbf{a} + \frac{\partial \mathrm{U}_0}{\partial \tau^*}\cdot v_n\right)\right]$$
$$\mathbf{a} = n_x\hat{i} + n_y\hat{j} + n_z\hat{k} \qquad (37)$$
$$\left(\frac{\partial \mathrm{U}}{\partial \tau^*}\right)_s = \left(\frac{\partial \mathrm{U}}{\partial t}\right)_s - v_n\left\{\mathbf{n}_x\left(\frac{\partial \mathrm{U}}{\partial x}\right)_s + \mathbf{n}_y\left(\frac{\partial \mathrm{U}}{\partial y}\right)_s + \mathbf{n}_z\left(\frac{\partial \mathrm{U}}{\partial z}\right)_s\right\}$$

Here, v_n is the shock normal velocity, τ^* is the time coordinate in imaginary computational domain with same value as physical time, i.e., $t = \tau^*$. u_n is the normal velocity and c is the velocity of sound in the flow field corresponding to the high pressure side of the marker points. $\mathrm{I_N}$ is the eigenvector for the characteristic field approaching the shock from behind with velocity (eigenvalue) $\left(u_n - v_n + c\right)$. Conservative flow-variables represented by $\mathbf{U}$ and flux vectors $\vec{\mathbf{F}} = \left(E, F, G\right)$ have same form as given by Eqs.(8)-(11). Subscripts 's' and '0' are used to denote a marker point's high pressure and low pressure sides respectively. The values of flow variables at the marker point are obtained by high-order interpolation. Thus along with Navier-Stokes equations, one needs to solve following system of equations to advance the front.

$$\frac{\partial v_n}{\partial \tau} = f\left(x_s, y_s, U_s, U_0, I_N\cdot\frac{\partial U_s}{\partial \tau}, v_n\right)$$
$$\frac{\partial x_s}{\partial \tau} = v_n n_x \qquad (38)$$
$$\frac{\partial y_s}{\partial \tau} = v_n n_y$$

Based on the shock velocity, marker points are moved to new locations and shock geometry updated. New intersection points with the grid-lines are found using a Newton-Raphson procedure and relation between grids and interface is updated. When shock-front moves, it can cross some grid points as shown Fig. 8. The solution at such grid points is no longer valid as they are on wrong side of the shock. Indicator values at such nodes are corrected and values of flow variables are obtained by interpolations from appropriate side of the shock. A simple Euler method of time stepping for this method will be as follows.

0. Initial condition (flow field and interface data known)
1. Find one-sided difference coefficients for irregular points

2. Find fluxes at all the grid points (regular as well irregular)
3. Find shock-acceleration in normal direction (based on Zhong, JCP-98).
4. Update values at all grid points from fluxes where they are calculated.
5. Move shock-front and make adjustments due to marker movements
    a. Update grid points where $\sigma < \sigma^*$
    b. Update grid points where $|\phi| > 1$
    c. Update shock-velocity for all interface points and advance markers.
    d. Obtain new marker points as intersection with grid-lines.
    e. Identify and update the grid-points that are crossed by shock-movement.
    f. Establish new correlations between grid and markers.
6. Advance time $t^{n+1} = t^n + dt$
7. Obtain flow field values at low-pressure side of marker points from interpolation.
8. Use Rankine-Hugoniot relations to obtain values on high-pressure side of marker points.
9. Apply boundary conditions.
10. If t<tend, go back to step 1.

5 FRONT-TRACKING RESULTS FOR SHOCK AND DISTURBANCE INTERACTION PROBLEM

In literature, results are available for small two-dimensional vorticity and entropy disturbances interacting with a shock which we have used for assessing utility of our shock-fitting algorithms for shock-turbulence interactions. These results are presented in this section.

Mahesh [16] carried out linear interaction analysis for two-dimensional problem of a normal Mach 1.5 shock interacting with weak plane vorticity-entropy waves traveling at varying angles of incidence. For this problem, the domain is assumed to contain an ideal gas with specific heat ratio 1.4. Fluctuations are superposed over steady Mach 1.5 normal shock solutions (obtained from the Rankine-Hugoniot relations) for the gas. Disturbances propagate downstream from the inflow boundary and interact with the normal shock as shown Fig. 9(a). The interactions of normal shock and disturbances cause time-periodic shock distortions and disturbance amplifications. We considered the post-shock solutions for this problem using conventional shock-fitting in past [1] and results were shown to be comparing really well with Linear Interaction Analysis results. In current study, we solve this problem by using our new front tracking based shock-fitting method and compare the result with conventional moving-grid shock-fitting results.

A stationary Mach 1.5 shock wave is perturbed at $t = 0.0$ by a small amplitude disturbance field of the incident plane wave that makes angle ψ_1 with the X- axis. The incident field has the following form:

$$\begin{aligned} u' &= U_1 A_v \sin\psi_1 \cos\left(k_x x_0 + k_y y - U_1 k_x t\right) \\ v' &= -U_1 A_v \cos\psi_1 \cos\left(k_x x_0 + k_y y - U_1 k_x t\right) \\ \rho' &= \rho_1 A_v \cos\left(k_x x_0 + k_y y - U_1 k_x t\right) \\ p' &= 0.0 \end{aligned} \tag{39}$$

where variables U and ρ denote the mean velocity and density respectively and The variables u', v', p' and ρ' represent fluctuations in velocities, pressure and density respectively. Subscripts 1 and 2 denote the upstream and downstream steady states. For the computations presented here, $k_y = k\sin\psi_1 = 1$ and $k_x = k\cos\psi_1$ is used. Perturbation are introduced at $x_0 = 0.0$ while initially shock is located at $x = 1.5\pi$. Length of domain in y direction $L_y = 2\pi$ ensures that at each x location the flow is periodic over the computation domain in Y direction. The variables used here were non-dimensionalized by appropriate combinations of reference length L_0^*, reference speed of sound c_0^* and reference density ρ_0^* corresponding to the unperturbed free-stream values. For the present study we used $A_v = A_e = 0.025$, i.e. vorticity and entropy waves in same phase were considered.

To implement the conventional moving-grid shock-fitting scheme, we divide the computational domain in two zones sharing the shock as common boundary as shown in Fig. 9(b). Since the flow behind the shock is subsonic we use non-reflecting boundary conditions with a buffer-zone. Periodic boundary conditions were used in Y-direction. The problem was also computed on fixed grids by solving Euler equations with our two-dimensional front-tracking adaptation of shock-fitting algorithm described in section 4. Shock is represented using marker points which are defined as intersections of shock-front with the grid-points as shown in Fig. 9(c). The shock thus defined can freely move over the underlying grid-points. Movement of shock-points is derived using the physics of problem.

As computations are started, large oscillations in flow properties are observed downstream of the shock along all values of Y coordinates. These transient disturbances propagate downstream followed by an oscillating field. Figure 10 shows transients in vorticity profiles moving downstream of the flow. Although, the shock profile becomes sinusoidal (Fig. 10(c)), the initial transients are still seen downstream of the shock (Figs. 10(a) and 10(b)). The exit boundary presents a problem for computation since flow is subsonic at the exit. Boundary conditions at the exit need to be chosen such that vorticity, acoustic and entropy perturbation in the domain are allowed to propagate properly otherwise such disturbances might reflect and contaminate the solution. We use approximately non-reflecting boundary conditions of Poinsot and Lele [51] at the outflow boundary and find that vorticity waves leave the domain and we obtain time periodic vorticity downstream of the shock. Figure 11 shows density contours and density profile after the transients leave the domain. It can be seen that a sinusoidal density profile is obtained along X direction. Moreover, the shock-interface itself is sinusoidal as expected from linear theory.

As a benchmark for validation of front-tracking results, we use the conventional shock-fitting algorithm but solve the flow-field ahead of the shock as well. For this, we use computational domain showed in Fig. 9(b). Both sides of shock are treated as separate zones with the shock as common boundary. Fifth-order upwind finite differencing is applied separately on both sides of the shock and shock-fitting algorithm is used to update the shock position. Results for post-shock flow obtained with moving grid shock-fitting algorithm were presented in our previous work [1] and were found to be very accurate when compared against the theoretical and numerical results obtained by Mahesh [16].

Figure 12 compares results from front-tracking and moving-grid based shock-fitting methods for 45˚ angle of incidence at $t = 10s$. We define nondimensional entropy S^* of the fluid at pressure, p and density (ρ) as follows:

$$S^* = \frac{\Delta s}{C_p} = \frac{\ln p}{\gamma} - \ln \rho \tag{40}$$

We see that front-tracking results match fairly well to those obtained from conventional shock-fitting results on moving-grids for all the variables in Fig. 12. Incoming waves of entropy (Fig. 12(a) and vorticity (Fig. 12(b)) remain sinusoidal even after crossing the shock. It should be noted that vorticity values use spatial derivatives in two directions and there may not be enough points for approximating spatial derivatives in both directions while using front-tracking method. Hence, some vorticity values around shock have not been plotted for front-tracking method in Fig. 12(b). Pressure profile in Fig. 12(c) also remain sinusoidal which is expected from linear theory as critical angle of incidence for this flow-field (66˚) is larger than actual angle of incidence. Amplitude of density fluctuation increases as shown in Fig. 12(d) which is in accordance with the linear theory. Figure 13 presents parameters relevant to interface geometry for the flow field corresponding to the results of Fig. 12. It can be seen from Fig. 13(a) that shock-profile is sinusoidal and shock moves through the underlying grid. Also, location and shape of shock from the front-tracking method agrees well to those obtained from the shock-fitting method on moving grids. Normal to the shock is found using a high-order iterative procedure as described in section 4. Shock-points are moved using shock-acceleration relations obtained from physics of the problem. It can be noted that variation of Y-component of interface-normal (Fig. 13(b)) and shock-velocity (Fig. 13(c)) are also sinusoidal as predicted by linear theory.

Similar to Figs. 12 and 13, Figs. 14 and 15 show results for 75˚ angle of incidence case. From Fig. 14, it can be seen that variations in flow variables from front-tracking method agree reasonably well to those obtained from moving-grid shock-fitting method. As compared to results for 45˚ angle of incidence, we see that entropy wave (Fig. 14(a)) and vorticity wave (Fig. 14(b)) have large wavelengths although they remain sinusoidal before and after the shock. Pressure (Fig. 14(c)), however, is an evanescent field as predicted by linear theory. Similarly, the interface data presented in Fig. 15 again shows that front-tracking method predicts location and geometry of the shock reasonably well.

Although results obtained from 2-D front-tracking were found to be satisfactory for the problem considered here, the algorithm may still be improved. The front-tracking algorithm was found to be very tedious to implement with high-order approximations. High-order implementation was found to be more prone to spurious numerical oscillations. For example, we compare in Fig. 16, 5th order front-tracking results with 3rd order front-tracking results for 75˚ angle of incidence case with $\sigma^* = 0.5$ instead of $\sigma^* = 1.0$ as used for Fig. 13. One can observe that 5th order results show numerical oscillations in density as well as vorticity values while 3rd order results match well to the moving-grid shock-fitting results. Moreover, we found that as amplitude of incoming wave is increased, conventional shock-fitting method is much more robust as compared to those from front-tracking method. Hence, for isotropic shock and turbulence interaction problems, we expect conventional shock-fitting in multi-zone setting to be more useful than current implementation of front-tracking method.

6 ASSESSMENT OF METHODS TO FIND SHOCK VELOCITY

An important part of the shock-fitting and shock-tracking methodology is to find accurate velocity of shock using the physics of the problem. Popular shock-fitting based methods derive a shock acceleration relation based on time derivative of Rankine-Hugoniot jump conditions and characteristic based flow-information from high-pressure side of the flow. We have previously shown this method to be fifth-order accurate in treating the flow behind the shock [1]. However, there can be several ways to find the shock velocity at a given point on interface. Since accurate computation of shock-location is of paramount importance to the shock-turbulence interaction problems, it is worthwhile to assess utilities of different methods of obtaining shock-velocities. To compare different methods, we choose a canonical problem involving one-dimensional interaction of shock and density disturbance and find the order of convergence. The problem was suggested by Suresh [52] and is given as:

At $t = 0$ for $x < 2.0$

$$\begin{aligned} \rho &= (\gamma+1)M^2 \Big/ \left[(\gamma-1)M^2+2\right] \\ u &= \gamma^{1/2}\left[2\left(M^2-1\right)\Big/\left\{(\gamma+1)M\right\} - M\right] \\ p &= 1 + 2\gamma\left(M^2-1\right)\Big/(\gamma+1) \end{aligned} \tag{41}$$

while for $x > 2.0$,

$$\begin{aligned} \rho_\infty &= 1.0 + \varepsilon \sin^4\left\{2.5\pi\left(x + M\gamma^{1/2}t\right)\right\} \\ u_\infty &= -M\gamma^{1/2} \\ p_\infty &= 1.0 \end{aligned} \tag{42}$$

If there is no disturbance, these relations correspond to a standing shock. We use a strong shock with M=3 , γ=1.4, ε=0.2 . ρ , γ , u , M and p represent density, ratio of specific heats for the gas, velocity, Mach number and pressure respectively. This problem is a modified form of more popular Shu-Osher problem and has been chosen since post shock flow for this problem have continuity in density as well as its first, second and third derivatives in space, thus making post-shock solution much smoother. The unsteady problem is computed till $t = 0.32$ so that shocklets are not formed behind the main shock. Thus the problem is expected to show true order of convergence for the shock-fitting method. To carry out the convergence analysis, we compute the unsteady problem for a number of grid-sets. A very fine grid solution, ($dx = 3.125e-4$) solution obtained with high order central difference scheme and conventional shock-acceleration method [1, 42] is taken as reference solution. The error values are obtained for different sets of grids and the approximate order of accuracy, n , is then defined as:

$$n = \log\left(\frac{e_{\Delta x}}{e_{\Delta x/2}}\right)\Big/\log(2) \tag{43}.$$

Where e_h represents error from reference solution for grid-spacing h . The computational domain used for these calculations is shown in Fig. 17. The problem was solved for three sets of grids

$$\begin{aligned} &\text{Grid-set 1: Spacing, } dx_1 = 2.5\times10^{-3} \text{ (No of grids, N=800)} \\ &\text{Grid-set 2: Spacing, } dx_2 = 1.25\times10^{-3} \text{ (No of grids, N=1600)} \\ &\text{Grid-set 3: Spacing, } dx_3 = 6.25\times10^{-4} \text{ (No of grids, N=3200)} \end{aligned} \tag{44}$$

Various methods for finding shock-velocity were considered for the results in this section while a 5th-order upwind central differencing scheme of Zhong [42] is used with RK-3 time-stepping.

6.1 Methods for Finding Shock-Acceleration

Conventional shock-fitting methods find the shock acceleration by taking time derivative of Rankine-Hugoniot conditions and using one characteristic equation similar to Eq. (37) . The shock acceleration equation is then used to find the shock-velocity and update the shock location. Effect of grid refinement for this method was reported in our previous study [1] and error values from reference solution is presented in Table 1. It can be seen that close to fifth order convergence is observed for conventional moving grid shock-fitting.

Table 1: L-1 errors from conventional shock-fitting[42] *for problem defined by (41) and (42)*

	Error I: e_{dx_1}	Error II: e_{dx_2}	Error III: e_{dx_3}	Order from I and II	Order from II and III
Density	1.02E-05	4.39E-07	1.63E-08	4.54129919	4.747224
Velocity	7.77E-07	2.43E-08	7.89E-10	4.99887	4.94489
Pressure	5.87E-06	1.89E-07	6.06E-09	4.958014	4.961402

Henrick et al. [44] describe a different method to find the shock acceleration, where time derivative of only momentum is used. Momentum in the normal direction to the shock is given by

$$\rho_s u_{ns} = \frac{\rho_0 (v_n - u_{n0}) \left\{ \gamma \left(\rho_0 (v_n - u_{n0}) u_{n0} - 2p_0 \right) + \rho_0 \left(2{v_n}^2 - 3 v_n u_{n0} + {u_{n0}}^2 \right) \right\}}{\gamma \left(2p_0 + \rho_0 (v_n - u_{n0})^2 \right) - \rho_0 (v_n - u_{n0})^2}, \tag{45}$$

where, u_n is the normal velocity to the shock and v_n is the velocity of the shock. Subscripts 's' and '0' are used to represent high-pressure side and low pressure side of the shock. One can take the derivative of Eq. (45) with respect to v_n and use following relation for shock acceleration

$$\frac{dv_n}{d\tau} = \left(\frac{\partial(\rho_s u_{ns})}{\partial \tau} \right) \bullet \left(\frac{\partial(\rho_s u_{ns})}{\partial v_n} \right)^{-1} \tag{46}$$

Here the term $\left(\frac{\partial(\rho_s u_{ns})}{\partial \tau} \right)$ is computed directly as one solves governing equation (16). This method is more general as compared to method of Henrick et al [44] as they solve one-dimensional governing equations in a reference frame fixed to the shock front. Figure 18 compares solutions from all three sets of grids obtained with Eq. (46) against the reference solution. It can be seen that as the grid is refined, density values approach to the reference solution. Comparing solutions from Fig. 18(b) and 18(c), it can be seen that convergence is generally not very good near the shock. A coarse grid result obtained from this alternative method is compared with the conventional method in Fig. 19. It is again observed that results obtained from conventional method are significantly better match to the reference values as compared to those obtained from Eq. (46). These error values are quantified in Table 2.

Table 2: L-1 errors of shock-fitting based on momentum-change, Eq. (46)

	Error I: e_{dx_1}	Error II: e_{dx_2}	Error III: e_{dx_3}	Order from I and II	Order from II and III
Density	9.66E-06	7.05E-07	1.21E-07	3.776791	2.540185
Velocity	2.00E-06	1.51E-07	2.44E-08	3.723481	2.628458
Pressure	1.57E-05	1.20E-06	1.93E-07	3.715074	2.634586

Thus, as compared to conventional shock-fitting method, error values are generally higher when shock is updated using Eq. (46). Moreover, as the grid is refined the rate of convergence is less than the expected order of accuracy. From these results, it can be deduced that the shock-acceleration method which uses time derivative of appropriate characteristic variable corresponding gives better results as compared to the one where only momentum equation is used.

6.2 A Method Based on Riemann invariants

An alternative to shock-acceleration based method is to compute the shock velocity directly using the value of Riemann invariant from behind the shock. For the unsteady one-dimensional problem considered here, a schematic of the movement of characteristics is shown

in Fig. 20. On C_+ line, given by $dx/dt = u + c$, we have Riemann invariant $J^+ = u + 2c/(\gamma - 1) = const$. This value of J^+ is related to upstream conditions as

$$\frac{J^+}{c} = \frac{2(M_1^2 - 1)}{(\gamma + 1)M_1} + \frac{u_\infty}{c} + \frac{2}{(\gamma - 1)}\sqrt{\left[1 + \frac{2\gamma(M_1^2 - 1)}{(\gamma + 1)}\right]\left[\frac{2 + (\gamma - 1)M_1^2}{(\gamma + 1)M_1^2}\right]} \qquad (47)$$
$$M_1 = (v_s - u_\infty)/c$$

where c is velocity of sound downstream of the shock and v_s is shock-velocity. Once J^+ value is known behind the shock, shock velocity can be found using an appropriate numerical method (e.g. Secant method) to solve Eq. (47). With known values of flow field, shock velocity v_s^n and shock location x_s^n at a particular time t_n, as shown in Fig. 20, one can find the velocity v_s^{n+1} at new time step, $t_{n+1} = t_n + \Delta t$, using following steps:

1. Advance the shock to new position $x_s^{n+1} = x_s^n + \Delta t \bullet v_s^n$.
2. Choose appropriate number of grid points (5 in current study) behind the shock at time t_n and find location of C_+ lines ($dx/dt = u + c$) originating at these points at time t_{n+1}. Values of Riemann invariant $J^+ = u + 2c/(\gamma - 1)$ at the chosen grid points is also computed and stored.
3. Using locations of C_+ lines originating from chosen grid points and corresponding J^+ values found in step 2, interpolate to obtain Riemann invariant behind the shock J_s^+ corresponding to x_s^{n+1} location.
4. With known value of J_s^+, solve Eq. (47) to obtain v_s^{n+1}.

Velocity of shock is obtained at the new time without the need of finding shock-acceleration values. This algorithm was implemented with our conventional moving grid shock-fitting code and problem given by Eqs. (41) and (42) was solved with fifth order central finite differencing for spatial derivatives and Rk-3 time stepping. Five grid points were used for interpolation in step 2. The density profiles are presented in Fig. 21 for these sets of grids and are compared with the reference profile. Fig. 21(a) shows that results compare well with the reference profile for all three grid-sets considered here. As we zoom on a portion away from the shock (Fig. 21(b)), we see that results are converging towards the reference values with grid refinement. Figure 21(c) shows effect of grid refinement on prediction of shock location. It is observed that for all the three grid-sets used in this study, there is a sudden jump in density from the shock point to the adjacent point. Such jump is not observed in the reference solution which advances the shock based on shock-acceleration formula. Location of shock can also be seen to be converging towards the reference value with grid-refinement. Convergence rate for this case is measured using (43) and is presented in Table 3.

Table 3: L-1 errors using Riemann invariants for finding shock-velocity

	Error I: e_{dx_1}	Error II: e_{dx_2}	Order from I and II
Density	5.69E-03	3.32E-03	0.777701
Velocity	1.23E-03	6.97E-04	0.8188
Pressure	9.57E-03	5.46E-03	0.810507
Shock-location	3.68E-04	1.30E-04	1.502324

Thus, method of determining shock-velocity based on Riemann invariant gives poor results as compared to those obtained from the shock acceleration formulation. A sudden jump is observed in the profiles near the shock since shock velocity can change abruptly as the values of flow variable change. Shock velocity is directly used in Rankine-Hugoniot jump conditions which lead to large changes in the values just behind the shock. Acceleration based shock-updating methods ensure that changes in shock-velocity are smoother and thus show expected order of convergence.

Hence, based on these results, we find that conventional shock-fitting way of advancing shock using characteristics based shock-acceleration relation is more accurate for unsteady shock disturbance interaction problems considered.

7 SHOCK-FITTING METHOD WITH WENO SCHEME

Current study focuses on solving canonical problem shown in Fig. 1, where a main shock interacts with incoming disturbances or turbulent flow. In past, we have shown that shock-fitting method coupled with upwind finite-differencing shows high convergence rates if the flow behind the shock is smooth enough. However, the high-order upwind scheme is not suitable if secondary shocks are present behind the fitted shocks. Since secondary shocks are often observed in the shock-turbulence interaction problems, it is worthwhile to consider shock capturing schemes to solve the post-shock flow.

As described in section 3.2 and demonstrated in Fig. 2, one-sided finite differencing is required to approximate the spatial derivatives on the nodes close to the shock while interior of the domain is treated by a WENO scheme. In this section, we consider different sets of such combinations to assess the convergence properties. Specifically, WENO5 scheme of Jiang and Shu[43] and WENO5M scheme of Henrick et al.[44] are considered along with following one-sided 5-point finite difference formulas near the shock.

$$\left.\frac{\partial f}{\partial x}\right|_{I=IL} \approx \frac{1}{12\Delta x}\left(3f_{IL-4}-16f_{IL-3}+36f_{IL-2}-48f_{IL-1}+25f_{IL}\right)$$
$$\left.\frac{\partial f}{\partial x}\right|_{I=IL-1} \approx \frac{1}{12\Delta x}\left(-f_{IL-4}+6f_{IL-3}-18f_{IL-2}+10f_{IL-1}+3f_{IL}\right) \quad (48)$$
$$\left.\frac{\partial f}{\partial x}\right|_{I=IL-2} \approx \frac{1}{12\Delta x}\left(f_{IL-4}-8f_{IL-3}+8f_{IL-1}-f_{IL}\right)$$

Henrick et al [44] suggest using following combination of one-sided approximation near the shock, which have also been considered to use with WENO5 and WENO5M in this study.

$$\left.\frac{\partial f}{\partial x}\right|_{I=IL} \approx \frac{1}{60\Delta x}\left(-12f_{IL-5}+75f_{IL-4}-200f_{IL-3}+300f_{IL-2}-300f_{IL-1}+137f_{IL}\right)$$
$$\left.\frac{\partial f}{\partial x}\right|_{I=IL-1} \approx \frac{1}{12\Delta x}\left(-f_{IL-4}+6f_{IL-3}-18f_{IL-2}+10f_{IL-1}+3f_{IL}\right) \quad (49)$$
$$\left.\frac{\partial f}{\partial x}\right|_{I=IL-2} \approx \frac{1}{60\Delta x}\left(-2f_{IL-5}+15f_{IL-4}-60f_{IL-3}+20f_{IL-2}-30f_{IL-1}-3f_{IL}\right)$$

Thus following four combinations of shock fitting and WENO schemes are considered

Scheme 1: WENO5 with shock-fitting and application of (48) near the shock
Scheme 2: WENO5 with shock-fitting and application of (49) near the shock
Scheme 3: WENO5M with shock-fitting and application of (48) near the shock
Scheme 4: WENO5M with shock-fitting and application of (49) near the shock

For convergence study, we solve the smoother version of Shu-Osher problem defined by Eqs. (41) and (42) using all the four schemes described above and compare the results with those obtained from fifth order central finite difference scheme of Zhong [42]. Table 4 presents L-1 error in density values for various schemes. It can be observed that choice of one-sided difference scheme i.e. Eq. (48) or Eq. (49) for the points close to the shock does not significantly alter the error in density values. However, using WENO5M instead of WENO5 does reduce the errors significantly. As described in section 3.2, WENO5M maps weights calculated in WENO5 scheme to the values that are closer to ideal weights. Thus, in smooth region WENO5M leads to smaller error. These errors, however, are larger than 7-point fifth order upwind central differencing scheme. It can also be observed that for both WENO schemes, solutions approach to the design accuracy of 5^{th} order as grid is refined while central differencing shows fifth order convergence even for coarser grids. Similar observations are made when convergence of velocity field is studied. However, error in velocity values is also affected by choice of one-sided difference scheme near the shock. In general, using one-sided five point stencils for all the three points behind the shock (Eq. (48)) gives slightly lesser errors in velocity as compared to those obtained by using Eq. (49). Moreover, velocity values are seen to be converging with design accuracy for both WENO schemes as well as central difference scheme even for coarser grid. Errors from WENO5M scheme are generally 3-5 times less as compared to those from WENO5.

Table 4: Convergence of density values using various schemes for problem given by (41) and (42)

	Error I: e_{dx_1}	Error II: e_{dx_2}	Error III: e_{dx_3}	Order from I and II	Order from II and III
5th Order Central	1.02E-05	4.39E-07	1.63E-08	4.54129919	4.747224
Scheme 1	1.04E-04	8.35E-06	3.00E-07	3.63372094	4.797872
Scheme 2	1.04E-04	8.36E-06	3.04E-07	3.64290661	4.781968
Scheme 3	3.33E-05	2.17E-06	4.55E-08	3.93826979	5.577517
Scheme 4	3.40E-05	2.18E-06	4.61E-08	3.96727522	5.559748
Pure WENO5	5.31E-03	2.67E-03	1.26E-03	0.99359335	1.079674

Table 5: Convergence of velocity field using various schemes for problem given by (41) and (42)

	Error I: e_{dx_1}	Error II: e_{dx_2}	Error III: e_{dx_3}	Order from I and II	Order from II and III
Central Differencing	7.77E-07	2.43E-08	7.89E-10	4.99886965	4.94489
Scheme 1	2.92E-06	1.21E-07	4.56E-09	4.59540322	4.726582
Scheme 2	3.78E-06	1.55E-07	5.90E-09	4.60633121	4.717143
Scheme 3	1.13E-06	3.70E-08	1.29E-09	4.92821096	4.836535
Scheme 4	1.44E-06	4.73E-08	1.69E-09	4.92547902	4.809022
Pure WENO5	2.84E-03	1.55E-03	7.14E-04	0.87120134	1.117991

Better insight for convergence is obtained by observing pointwise errors. Spatial variations of point-wise errors in density values obtained for grid-spacings dx_1 and dx_2 are compared in Fig. 22 for central differencing scheme, WENO5 (Scheme 1) and WENO5M (Scheme 3) schemes. It can be observed that errors for finer grid are significantly less. Since log of error values on base 2 is plotted, one can deduce the local order of convergence, as defined in Eq. (43) , by taking difference between the any two profiles in Fig. 22. It can be seen that for all the schemes, errors incurred in the region just behind the shock is higher. Since the wavelength of the amplified disturbance is lesser in the region just behind the shock, lesser resolution is obtained in that region. For both the WENO schemes, pointwise errors generally correspond to accuracy between 3^{rd} and 4^{th} order while errors for central differencing correspond to mostly between 4^{th} and 5^{th} orders of accuracy. Errors for WENO schemes are significantly higher than central differencing for the grid-sets considered here. Figure 23 plots the spatial variation of pointwise errors in velocity values. While errors from central differencing scheme do not change a lot behind the shock, WENO schemes still show more errors near the shock. This is an effect of sharper variation in density profile just behind the shock affecting the smoothness indicators in WENO scheme. The errors indicate 4^{th} to 5^{th} order convergence for all the schemes, although errors are higher for WENO schemes.

The problem was also solved by pure WENO schemes alone and error values are tabulated in Tables 4 and 5. It can be observed that errors are generally much larger with pure WENO schemes as compared to the shock-fitting based methods. Moreover, only first order convergence is found in the solution for density as well velocity values. Figure 24 compares density profiles obtained from WENO scheme with (Scheme 1) and without shock-fitting for this problem. It can be observed that, for this 1-D problem of almost standing shock, some post shock oscillations are observed (Fig. 24(b)) when flow is solved by purely WENO scheme which leads to deterioration of accuracy. From Fig. 24(c) it can be observed that even a coarse grid solution from shock-fitting is better than highly resolved purely WENO scheme. Thus, for simple one-dimensional problem there is obvious advantage of using shock-fitting algorithm as compared to using purely shock capturing schemes.

Canonical problem described by Eq.(39) provides a good test case to compare shock-capturing and shock-fitting algorithms. As described in section 5, a vorticity-entropy disturbance interacts with a normal Mach 1.5 shock. To implement the shock-fitting scheme, we divide the computational domain in 2 zones sharing the shock as common boundary as shown in Fig. 9(b). The problem was solved using WENO5 scheme with and without shock-fitting algorithm and density contours for angle of incidence of $75°$ are presented in Fig. 25(a). Diffused shock can be noticed for the case when pure WENO is used for the entire domain. Contours match fairly well except at the exit which could be due to exit boundary conditions. However, when we compare the density variation along X-direction, as done in Fig. 25(b), spurious numerical oscillations are observed for pure WENO scheme, while shock-fitting algorithm coupled with WENO as well as central differencing scheme provides very smooth solution.

Thus, combined shock-fitting and shock-capturing algorithms are much more accurate than using only shock-capturing schemes. Although accuracy is slightly poorer as compared to shock-fitting results with central differencing scheme, shock-capturing provides more robustness for when secondary shocks are formed behind the fitted shock.

8 SUMMARY AND FUTURE WORK

We have carried out a number of computations relevant to problems of shock and turbulence interactions. Specifically, our approach is to treat the shock as a sharp entity whenever possible using methods based on shock.-fitting algorithms. In conventional shock-fitting algorithm, flow is solved on the moving grid attached to the shock. For two-dimensional flows, we have been able to extend the idea of shock-fitting for computations with fixed grid while shock is tracked using front tracking method. Satisfactory results were obtained for canonical two dimensional shock and disturbance interaction problems. However, this method was found to be much more tedious to implement as compared to the conventional shock-fitting methods and high order implementation were prone to numerical instabilities. On the other hand, conventional shock-fitting method in multi-zone setting was found to be more robust and accurate. Considering the fact that main shock generally does not break down in the shock and isotropic turbulence interaction problems, it makes sense to take advantage of accuracy afforded by fitting the main shock instead of using shock-capturing in entire domain. However, complex interactions of high Mach number turbulence flow and shock might lead to nonlinearities, e.g. weak secondary shocks, in the post-shock flow. Hence, it is advisable to couple the moving grid shock-fitting method with shock-capturing schemes.

We have combined our conventional shock-fitting method with a couple of WENO schemes and found that expected order of accuracy is obtained in the flow behind the main shock for canonical unsteady shock and disturbance interaction problems. Moreover, results from coupled shock-fitting and WENO schemes were found to be much superior to those obtained from using pure WENO alone. Errors from pure WENO scheme were seen to be much larger than shock-fitting based schemes, e.g. for $dx = 2.5e-3$, density errors from pure WENO schemes are almost 20 times of those from shock-fitting errors. The disparity further grows as we refine the grid as pure WENO scheme showed only first order accuracy in the post shock flows and numerical oscillations were also observed.

We have also looked into some alternative methods for finding shock-velocity to improve efficiency and accuracy of front-tracking and shock-fitting algorithms. Results for these alternative methods were presented in the study and were found to be poor as compared to the conventional shock-fitting.

Based on the encouraging validation studies presented in this study, in future, we intend to explore problems involving interactions of shock and isotropic turbulence. The shock-fitting schemes combined with shock-capturing schemes are especially useful for high Mach number flows, since shock-fitting does not need grid stretching to capture the shock.

9 ACKNOWLEDGEMENTS

This research is supported by DOE Office of Science as part of a SciDAC (Scientific Discovery through Advanced Computing) project with “Science Application” in Turbulence with Dr. Lali Chatterjee as program manager. The authors would like to thank Prof. S. K. Lele and Prof. P. Moin of the Stanford University; Drs. A. Cook, W. Cabot, B. Sjögreen of the Lawrence Livermore National Laboratory and Dr. H. C. Yee of the NASA Ames Research Center for their valuable suggestions during the course of this work.

REFERENCES

1. Rawat, P., and Zhong, X. *Numerical Simulations of Strong Shock and Disturbance Interactions Using High-Order Shock-Fitting Algorithms*. *AIAA paper 2008-0746*. 2008.
2. Lee, T.K., and Zhong, X., *Spurious numerical oscillations in simulation of supersonic flows using shock-capturing schemes*. AIAA Journal, 1999. **37**(3): p. 313-319.
3. Kovasznay, L.S.G., *Turbulence in supersonic flow*. Journal of the Aeronautical Sciences, 1953. **20**(10): p. 657-682.
4. Chu, B.T., and Kovasznay, L. S. G., *Nonlinear interactions in a viscous heat-conducting compressible gas*. Journal of Fluid Mechanics, 1958. **3**: p. 494-514.
5. Ribner, H.S., *Convection of a pattern of vorticity through a shock wave*. NACA TN-2864 (Also as NACA Report 1164 1953), 1953.
6. Ribner, H.S., *Shock-turbulence interaction and the generation of noise*. NACA TN-3255 (Also as NACA Report 1233), 1954.
7. Ribner, H.S., *Acoustic energy flux from shock-turbulence interaction*. Journal of Fluid Mechanics, 1969. **35**: p. 299-310.
8. Moore, F.K., *Unsteady oblique interaction of a shock wave with a plane disturbances*. NACA TN-2879 (Also as NACA Rep. 1165), 1953.
9. Kerrebrock, J.L., *The interaction of flow discontinuities with small disturbances in a compressible fluid*, in *Mechanical Engineering*. 1956, California Institute of Technology: Pasadena, CA.
10. McKenzie, J.F., and Westphal, K. O., *Interaction of linear waves with oblique shock waves*. Physics of Fluids, 1968. **11**: p. 2350-2362.
11. Goldstein, M.E., *Turbulence generated by the interaction of entropy fluctuations with non-uniform mean flows*. Journal of Fluid Mechanics, 1979. **93**: p. 209-224.
12. Lee, L., Moin, P., and Lele, S. K., *Interaction of isotropic turbulence with a shock wave*. Report TF-52. Dept. Mech. Eng., Stanford Univ., CA, 1992.
13. Lee, L., Lele, S. K., and Moin, P., *Direct numerical simulation of isotropic turbulence interacting with a weak shock wave*. Journal of Fluid Mechanics, 1993. **251**: p. 533-562.
14. Lee, L., Lele, S. K., and Moin, P., *Interaction of isotropic turbulence with a strong shock wave*. AIAA Paper 94-0311, 1994.
15. Mahesh, K.A., Lee, L., Lele, S. K., and Moin, P., *The interaction of an isotropic field of acoustic waves with a shock wave*. Journal of Fluid Mechanics, 1995. **300**: p. 383-407.
16. Mahesh, K.A., Moin, P., and Lele, S. K., *The interaction of a shock wave with a turbulent shear flow*. Report TF-69, Thermosciences Division, Mechanical Engineering Department, Stanford University, 1996.
17. Mahesh, K.A., Lele, S. K., and Moin, P., *The influence of entropy fluctuations on the interaction of turbulence with a shock wave*. Journal of Fluid Mechanics, 1997. **334**: p. 353-379.
18. Fabre, D., Jacquin, L., Garnier, E., and Sagaut, P. . *Linear interaction analysis: The effect of a shock wave on a homogeneous perturbation field and on an entropy spot*. in *High Speed Compressible Flows, Euromech 403*. 1999. Poitiers.
19. Fabre, D., Jacquin, L., and Sesterhenn, J., *Linear interaction of a cylindrical entropy spot with a shock*. Journal of Physics of Fluids A, 2001. **13**(8): p. 2403-2422.
20. Pao, S.P., and Salas, M. D., *A numerical study of two-dimensional shock vortex interaction*. AIAA Paper 81-1205, 1981.
21. Zang, T.A., Hussaini, M. Y., and Bushnell, D. M. , *Numerical Computations of Turbulence Amplification in Shock-Wave Interactions*. AIAA Journal, 1984. **22**(1): p. 13-21.
22. Hussaini, M.Y., Kopriva, D., Salas, M. D., and Zang, T. A., *Spectral methods for the Euler equations. II - Chebyshev methods and shock fitting*. AIAA Journal, 1987. **23**: p. 234-240.
23. Meadows, K.R., Kumar, A., and Hussaini, M. Y., *Computational Study on the Interaction between a vortex and a shock Wave*. AIAA Journal, 1991. **29**(2): p. 174-179.
24. Meadows, K.R., and Casper, J., *Computing unsteady shock waves for aeroacoustic applications*. AIAA Paper 1993-4329, 1993.
25. Grasso, F., and Pirozzoli, S. , *Shock-wave-vortex interactions: shock and vortex deformations, and sound production*. Theoretical and Computational Fluid Dynamics, 1993. **13**(6): p. 421-456.
26. Andreopoulos, Y., Agui, J. H., and Briassulis, G., *Shock wave-turbulence interactions*. Annual Review of Fluid Mechanics 2000. **32**: p. 309-345.

27. Hannappel, R., and Friedrich, R., *Direct numerical simulation of a Mach 2 shock interacting with isotropic turbulence.* Applied Scientific Research, 1995. **54**: p. 205-221.
28. Jamme, S., Cazalbou, J. B., Torres, F., and Chassaing, P., *Direct numerical simulation of the interaction between a shock wave and various types of isotropic turbulence.* Flow, Turbulence and Combustion, 2202. **68**: p. 227-268.
29. Adams, N.A., and Shariff, K., *A high-resolution hybrid compact-ENO scheme for shock turbulence interaction problems.* Journal of Computational Physics, 1996. **127**(27): p. 57-.
30. Adams, N.A., and Shariff, K., *Direct numerical simulation of turbulent compression corner flow.* Theoretical and Computational Fluid Dynamics, 1998. **12**: p. 109-129.
31. Pirozzoli, S., *Conservative hybrid compact-WENO schemes for shock-turbulence interaction.* Journal of Computational Physics, 2002. **178**(1): p. 81-117.
32. Ducros, F., Ferrand, V., Nicoud, F.,Weber, C., Darracq, D., Gacherieu C., and Poinsot, T., *Large eddy simulation of the shock/turbulence interaction.* Journal of Computational Physics, 1999. **152**: p. 517-549.
33. Yee, H.C., Sandham, N .D., and Djomehri, M. J. , *Low dissipative high-order shock capturing methods using characteristic based filters.* Journal of Computational Physics, 1999. **150**: p. 199-238.
34. Sjogreen, B., and Yee, H. C., *Multiresolution wavelet based adaptive numerical dissipation control for high order methods.* Journal of Scientific Computing, 2004. **20**(2): p. 211-215.
35. Cook, A.W., Cabot, W. H., Welcone, M. L., Williams, P. L., Miller, B. J., de Supinski B. R., and Yates, R. K., *Tera-scalable algorithms for variable-density elliptic hydrodynamics with spectral accuracy.* LLNL report no. UCRL-CONF-211384, 2005, 2005.
36. Ma, Y., and Zhong, X., *Receptivity of a Supersonic Boundary Layer over a Flat Plate. Part 3: Effects of Different Types of Free-Stream Disturbances.* Journal of Fluid Mechanics, 2005. **532**: p. 63-109.
37. Ma, Y., and Zhong, X., *Receptivity of a Supersonic Boundary Layer over a Flat Plate. Part 1: Wave Structures and Interactions.* Journal of Fluid Mechanics, 2003. **488**: p. 31-78.
38. Ma, Y., and Zhong, X., *Receptivity of a Supersonic Boundary Layer over a Flat plate. Part 2: Receptivity to Freestream Sound.* Journal of Fluid Mechanics, 2003. **488**: p. 79-121.
39. Wang, X., and Zhong, X., *Numerical Simulation and Experiment Comparison of Leading-Edge Receptivity of A Mach 5.92 Boundary Layer*, in *44th AIAA Aerospace Sciences Meeting and Exhibit*. 2006, AIAA paper 2006-1107.
40. Sesterhenn, J., *Direct numerical simulation of the interaction of isotropic turbulence with a shock wave using shock-fitting.* Comptes rendus. Mecanique [1631-0721], 2005. **333**(1): p. 87-93.
41. Carpenter, M.H., and Casper, J. H., *Accuracy of shock capturing in two spatial dimensions.* AIAA Journal, 1999. **37**(9): p. 1072-1079.
42. Zhong, X., *High-order finite-difference schemes for numerical simulation of hypersonic boundary-layer transition.* Journal of Computational Physics, 1998. **144**: p. 662-709.
43. Jiang, G.S., and Shu, C. W., *Efficient implementation of weighted ENO schemes.* Journal of Computational Physics, 1996. **126**(1): p. 202-228.
44. Henrick, A.K., Aslam,T.D., and Powers, J. M., *Simulations of pulsating one-dimensional detonations with true fifth order accuracy.* Journal of Computational Physics, 2005. **213**(1): p. 311-329.
45. Roe, P.L., *Approximate Riemann solvers, parameter vectors, and difference schemes.* Journal of Computational Physics, 1981. **43**(2): p. 357-372.
46. Peskin, C., *The immersed boundary method.* Acta Numerica, 2002: p. 479-527.
47. Zhong, X., *A new high-order immersed interface method for solving elliptic equations with imbedded interface of discontinuity.* Journal of Computational Physics, 2007. **225**(1): p. 1066-1099.
48. Fedkiw, R.P., Aslam,T.D., and Xu, S., *The Ghost Fluid Method for deflagration and detonation discontinuities.* Journal of Computational Physics, 1999. **154**(2): p. 393-427.
49. Unverdi, S.A., and Tryggvason, G. , *A front-tracking method for viscous, incompressible, multi-fluid flows.* Journal of Computational Physics, 1992. **100**(1): p. 25-37.
50. Zhong, X., *A new high-order immersed interface method for multi-phase flow.* AIAA paper 2006-1294, 2006.
51. Poinsot, T.J., and Lele, S. K., *Boundary conditions for direct simulations of compressible viscous flow.* Journal of Computational Physics, 1992. **101**(1): p. 104-129.
52. Suresh, A., *Interaction of a shock with a density disturbance via shock fitting* Journal of Computational Physics, 2005. **206**: p. 6-15.

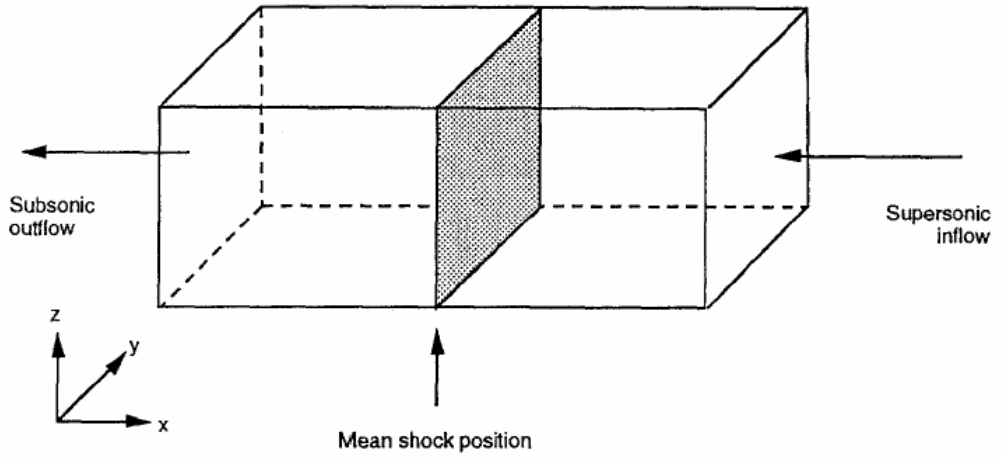

Fig. 1: A schematic of typical setting of isotropic shock and turbulence interaction.

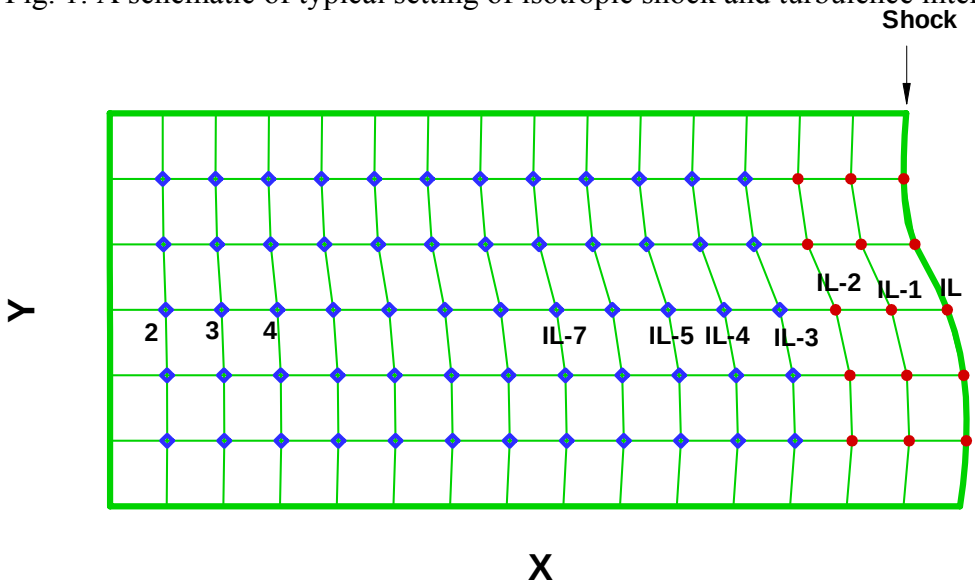

Fig. 2: For application of shock-fitting with 5th order WENO schemes, upwind finite differencing is used for points close to shock (shown by filled circles) while WENO scheme is applied for the interior (shown by hollow circles).

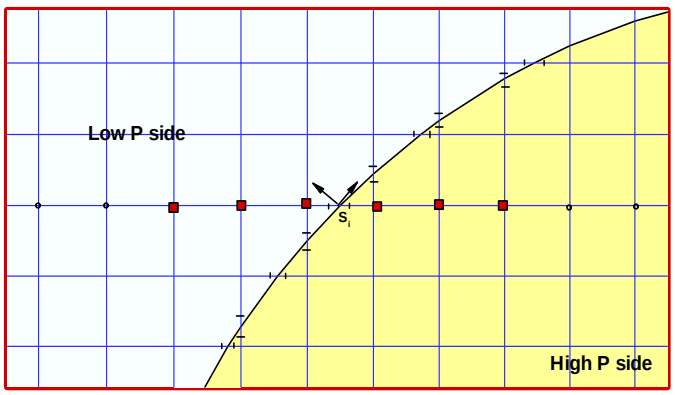

Fig. 3: Irregular points for 5th order front-tracking based fixed grid shock-fitting.

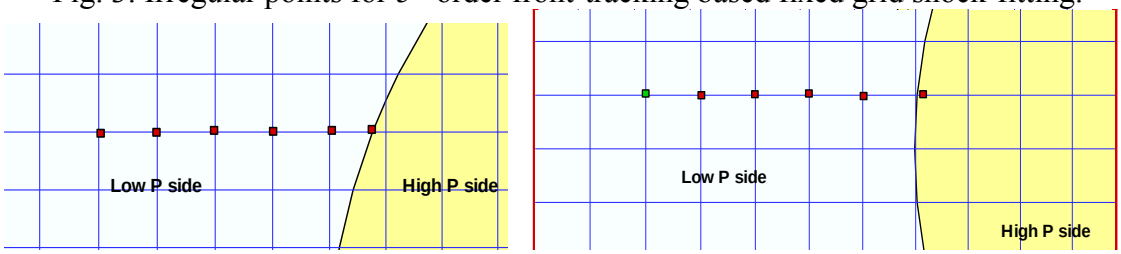

(a) (b)

Fig. 4: For one-sided difference derivatives not computed point closest to interface and an extra point (green) is included for interpolation.

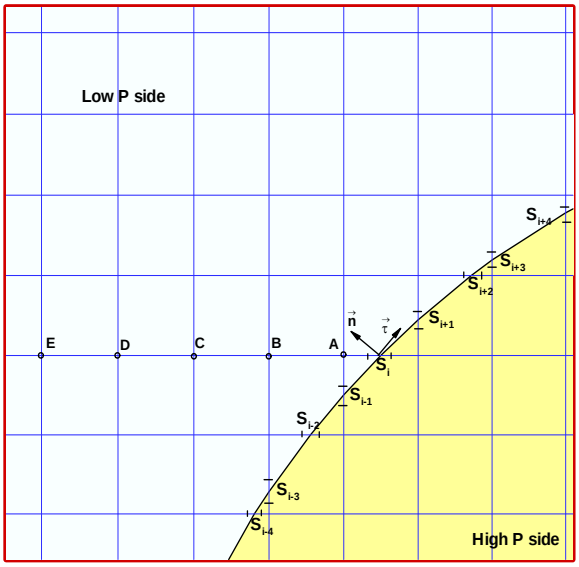

Fig. 5: Schematic for arrangement of Marker Points and stencil for one-sided differentiation for the fixed-grid-shock-fitting methodology.

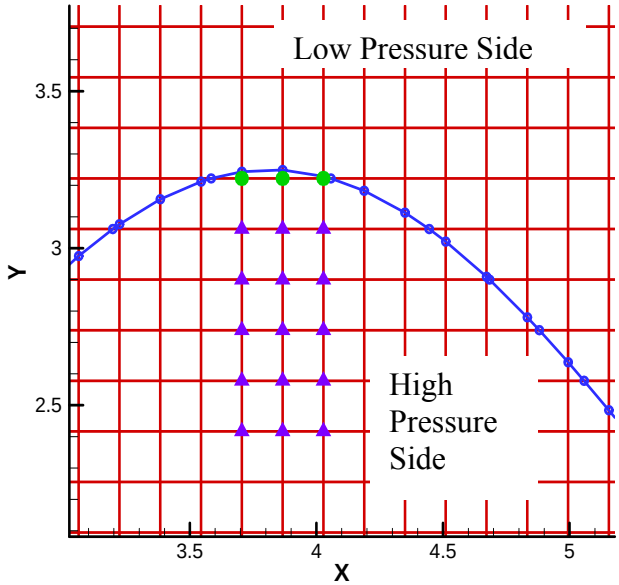

Fig. 6: Treatment of grid-points where enough points are not available for taking one-sided difference in X-direction ($\phi = -2$), shown by green circles. For such points, interpolation is carried out using neighboring grid-points Y-direction, shown by purple triangles.

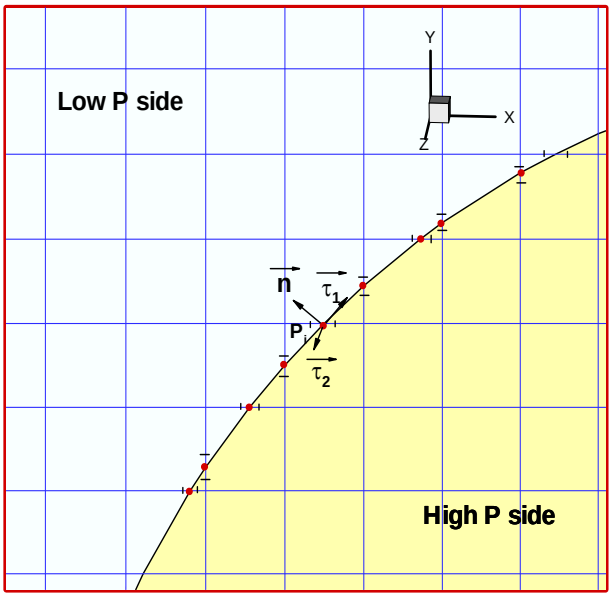

(a)

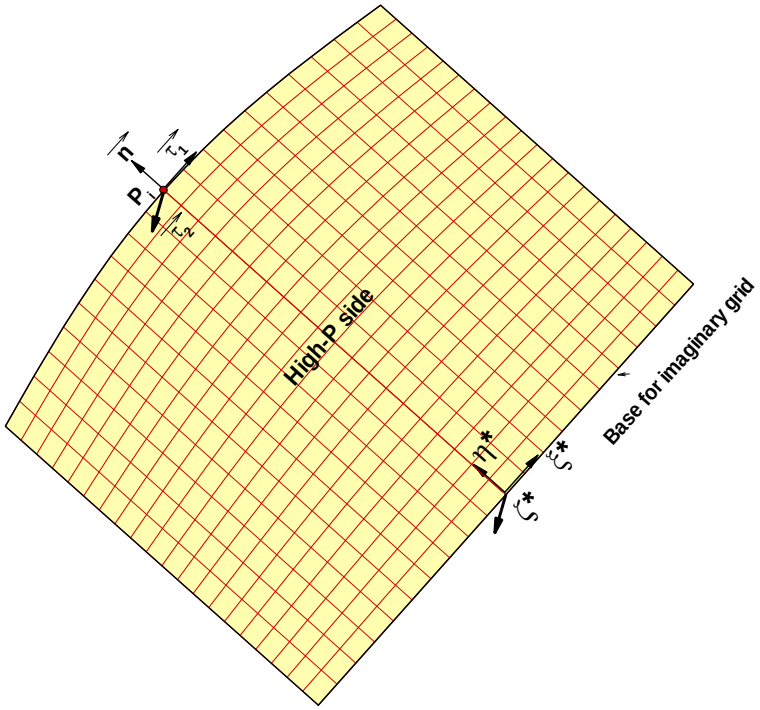

(b)

Fig. 7: Computation of shock velocity at a marker point in front tracking based fixed set-up shown in (a) is carried out by using appropriate values for an imaginary shock-aligned moving grid set-up as shown in (b).

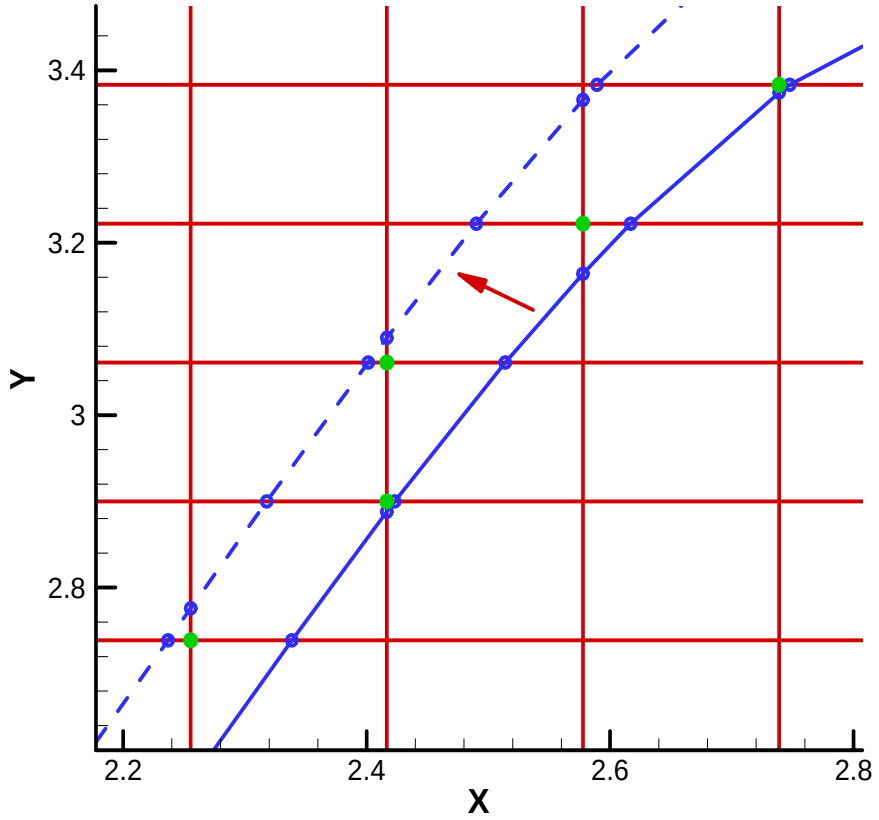

Fig. 8: Grid points crossed (highlighted by green dots) by movement of shock-front from old position from (solid blue line), to a new position (dashed blue line). New values at such grid-points are required as they are on wrong side of the shock with shock-movement.

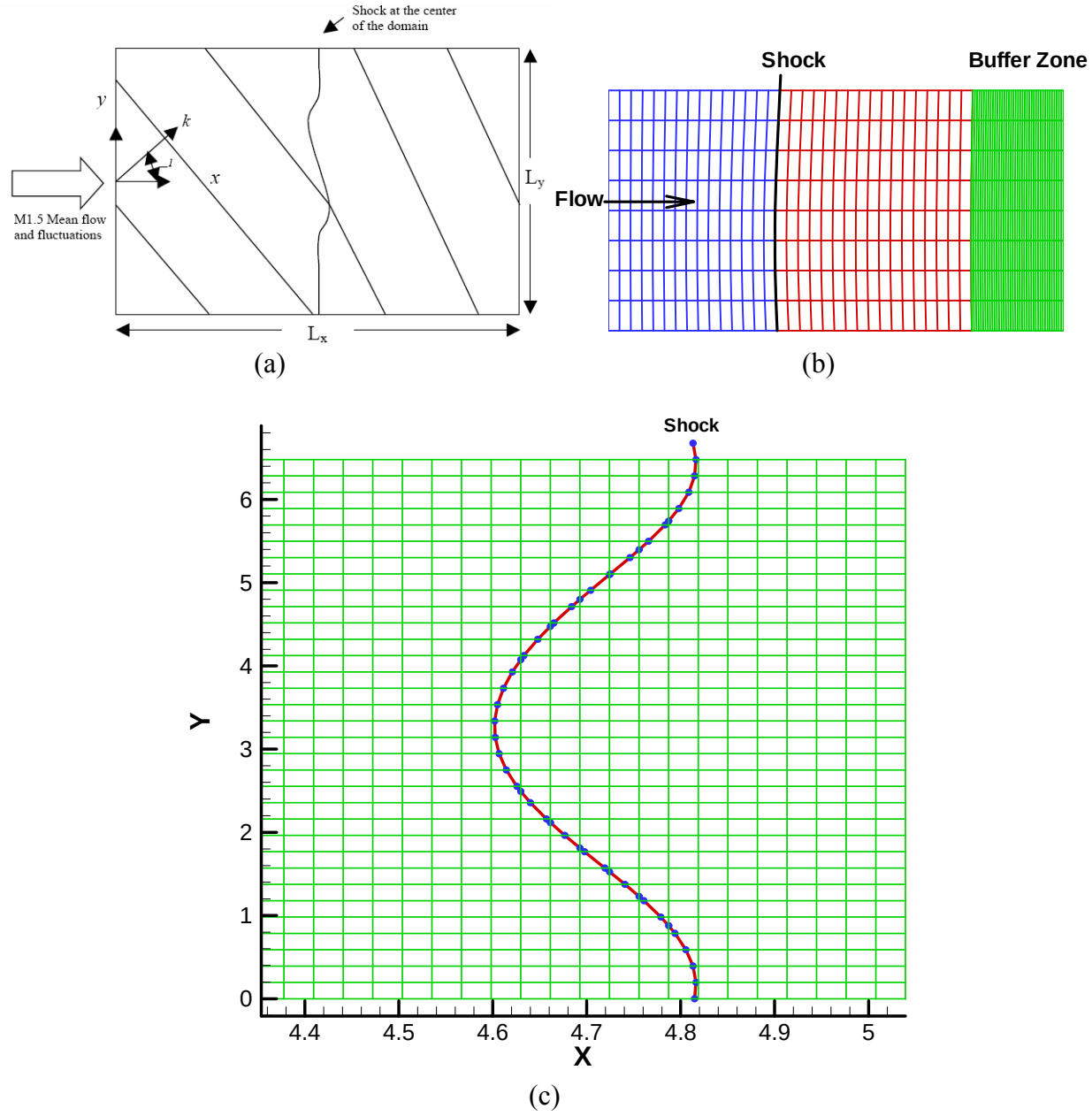

Fig. 9: For the shock and vorticity-entropy wave interaction (a) Schematic of the problem (b) Computational domain used for multi-zone moving grid shock-fitting and (c) Typical (fixed) grids and shock-profile corresponding to the Front-tracking based adaptation of shock-fitting algorithm. Shock passes through grid points where oscillations in shock can be noticed.

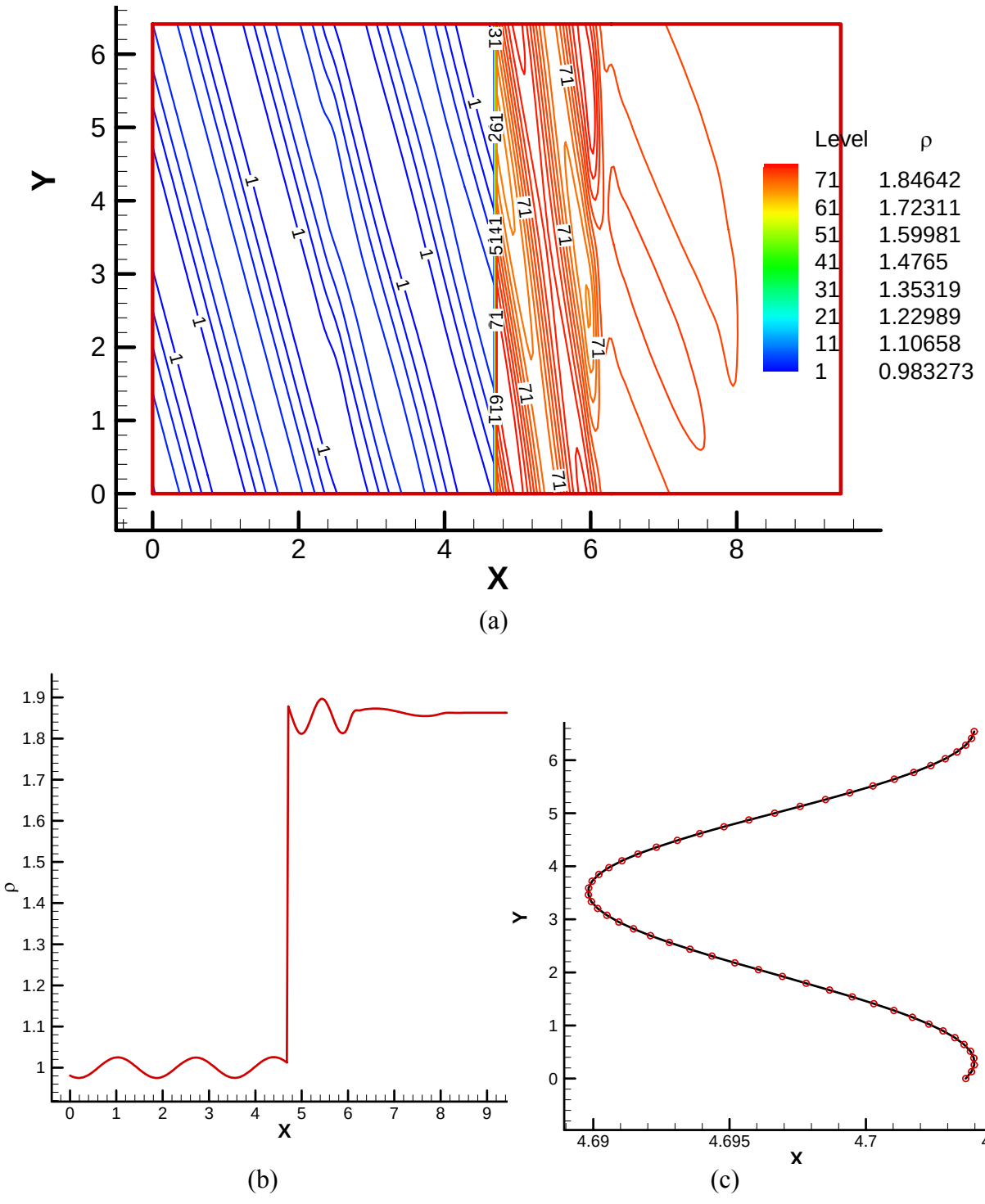

Fig. 10: Interaction of a vorticity-entropy wave at t = 4.0 after start. (a) Contours of density (b) Variation in X-direction at Y = π (centerline of domain) and (c) Interface shape with marker points for 15˚ angle of incidence

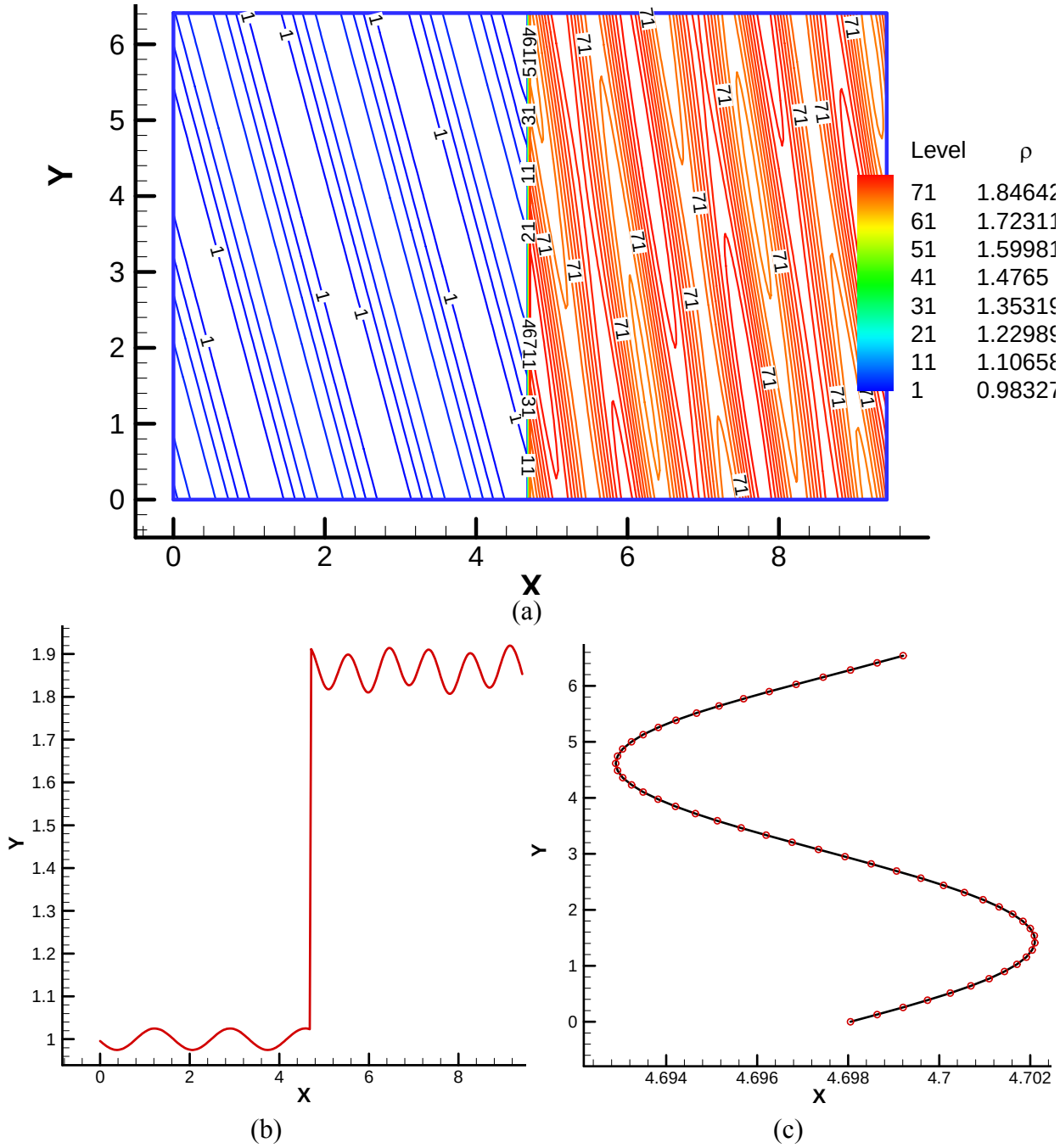

Fig. 11: Interaction of a vorticity-entropy wave at t = 10.0 after start. (a) Contours of density (b) Variation in X-direction at Y = π (centerline of domain) and (c) Interface shape with marker points for 15˚ angle of incidence.

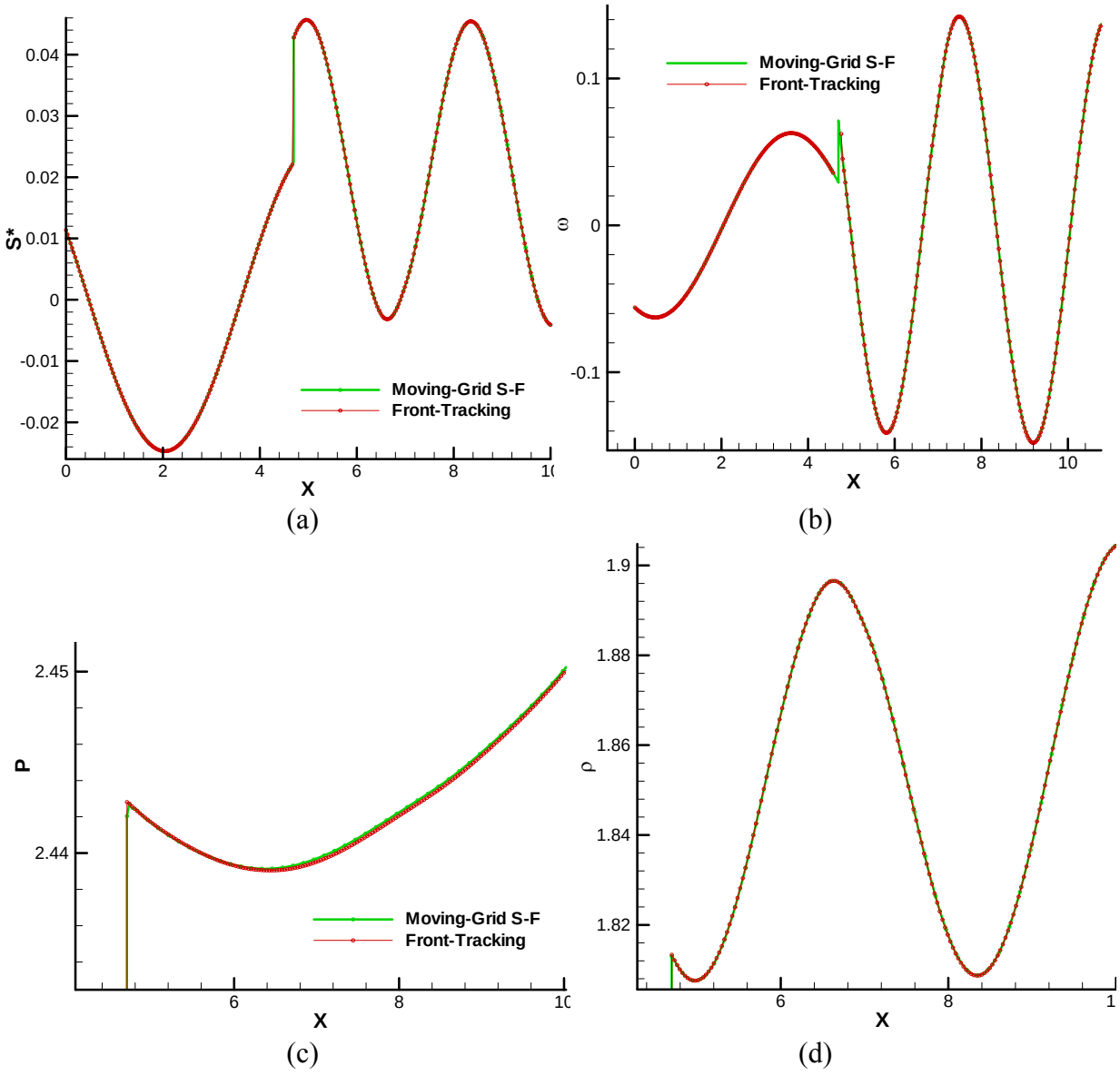

Fig. 12: Comparison of results from conventional shock-fitting and fixed-grid shock-fitting for variation in X-direction of (a) entropy (b) vorticity (c) pressure and (d) density at Y = π (centerline of domain) for 45˚ angle of incidence at $t = 10s$.

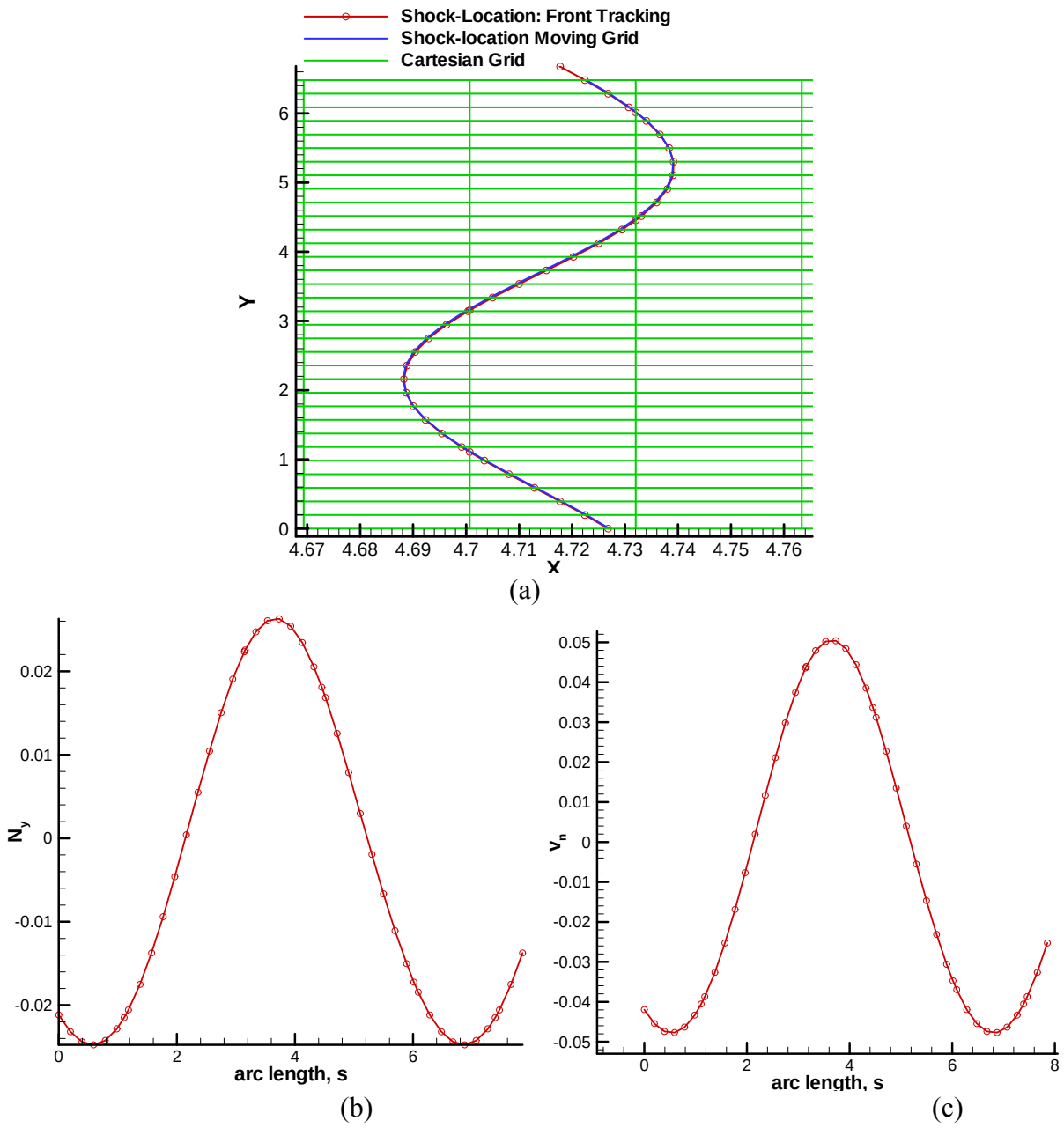

Fig. 13: Interface variables for 45˚ angle of incidence case obtained with Front-Tracking method (a) Location of the front on Cartesian grid compared with shock-location from moving-grid shock-fitting method (b) Y-component of the front-normal and (c) shock-normal velocity.

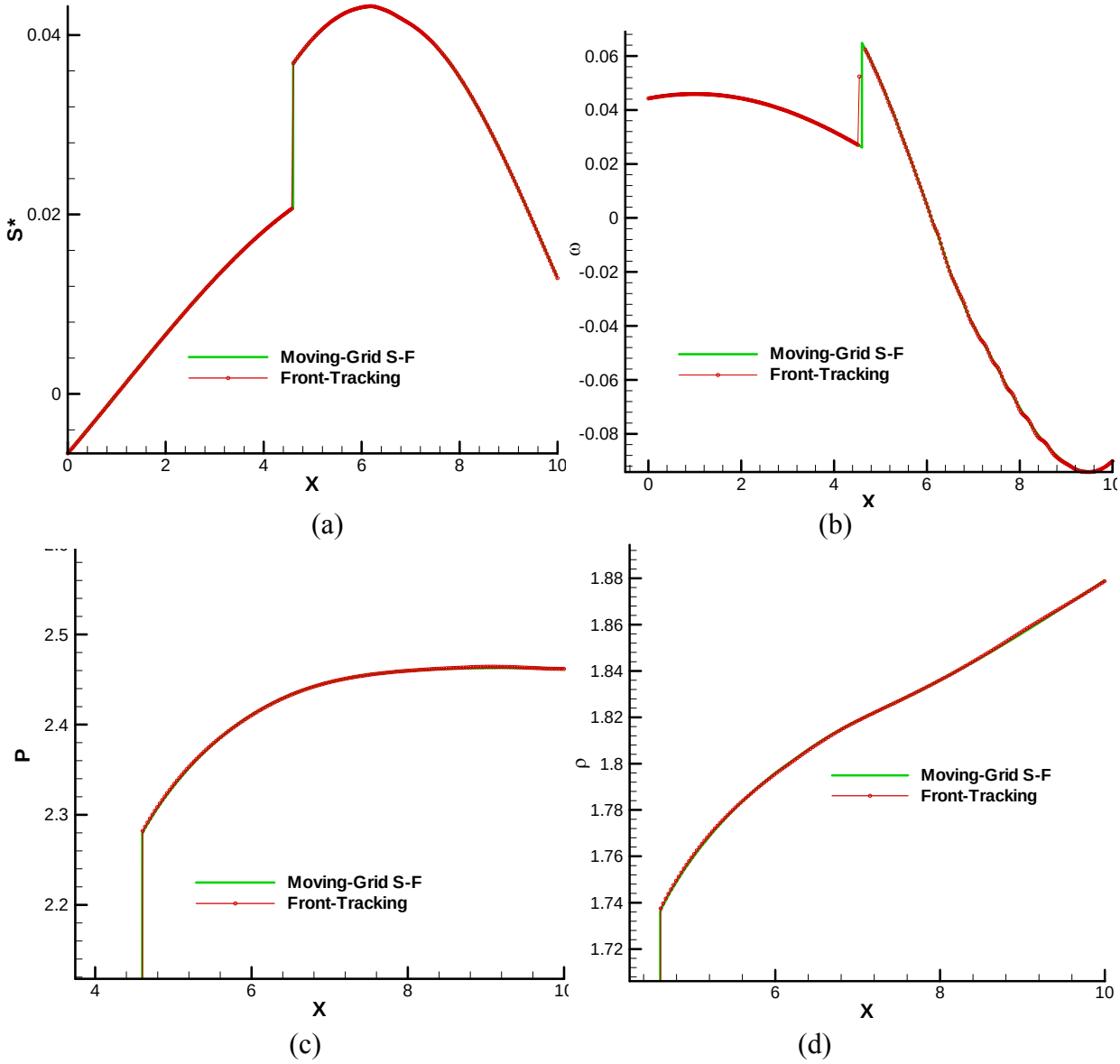

Fig. 14: Comparison of results from conventional shock-fitting and fixed-grid shock-fitting for variation in X-direction of (a) entropy (b) vorticity (c) pressure and (d) density at $Y = \pi$ (centerline of domain) for 75˚ angle of incidence at $t = 10s$.

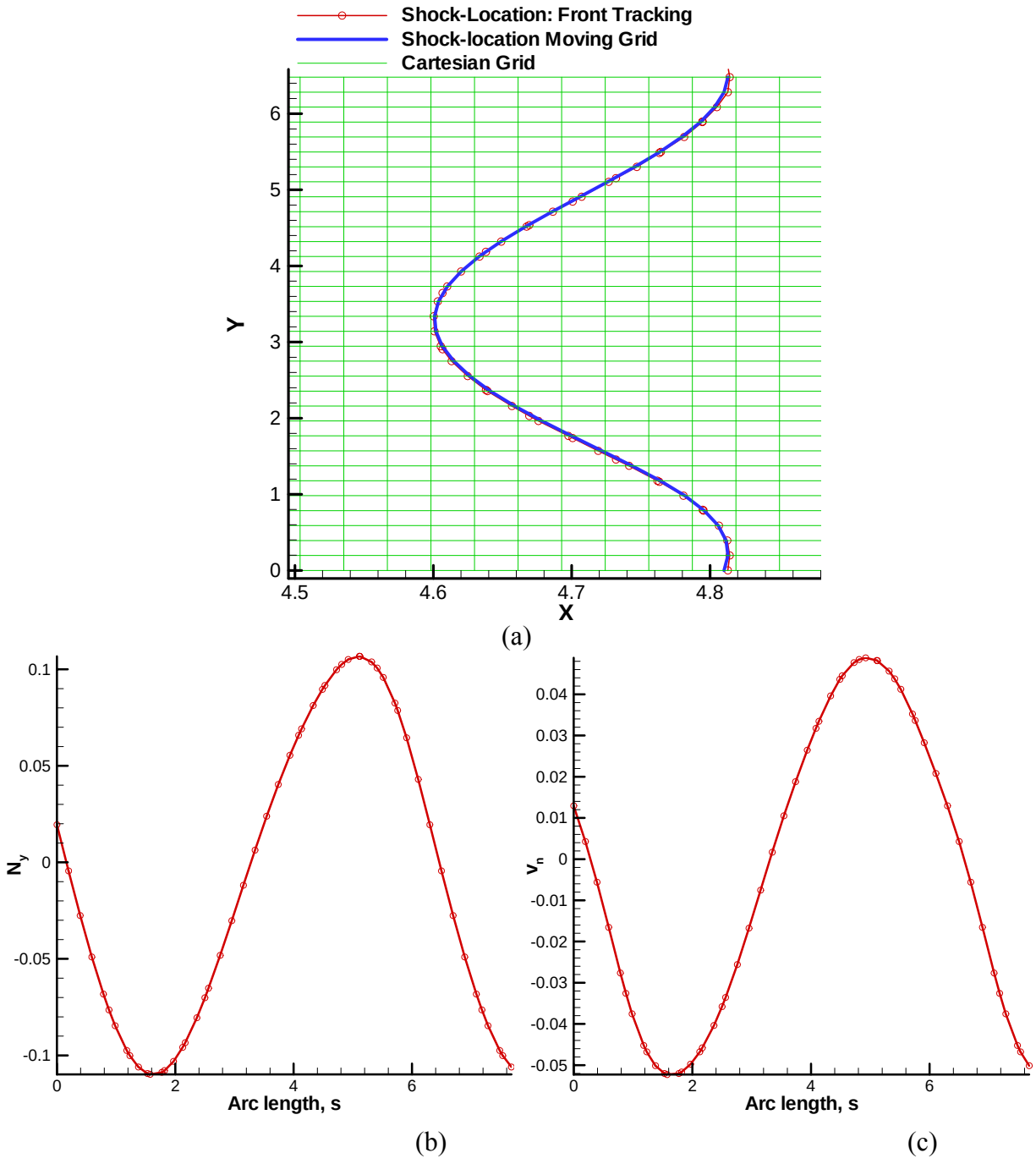

Fig. 15: Interface data for 75˚ angle of incidence case obtain with Front-Tracking method (a) Location of the front on Cartesian grid compared with shock-location from moving-grid shock-fitting method (b) Y-component of the front-normal and (c) shock-normal velocity.

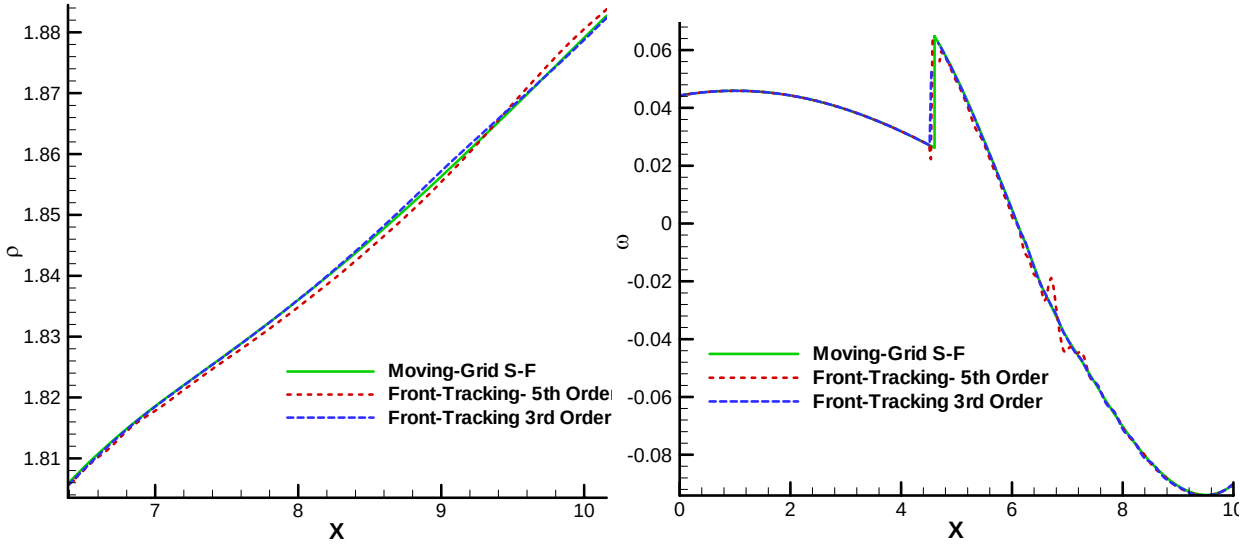

(a) (b)

Fig. 16: (a) Density and (b) vorticity variation along $Y = \pi$ line obtained from 5th order and 3rd order Front-Tracking methods and 5th order moving grid shock-fitting method for the shock-vorticity wave interaction at 75˚ angle of incidence.

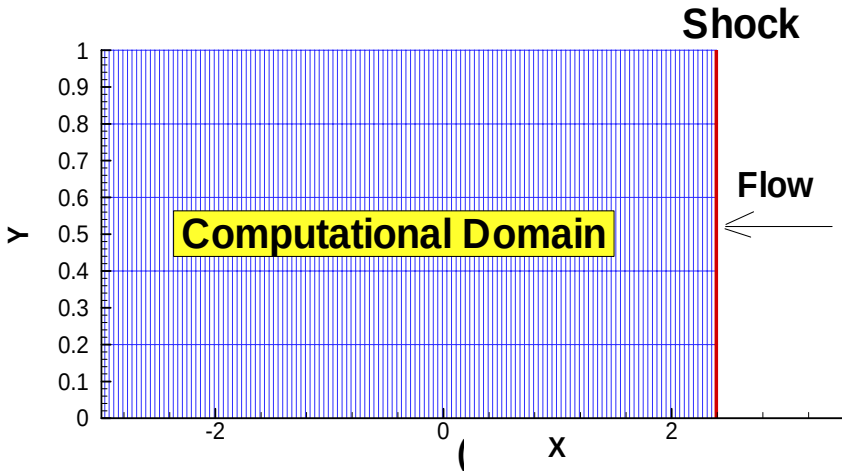

Fig. 17: Computational domain used for solving 1-D interaction of shock and density disturbance using conventional shock-fitting.

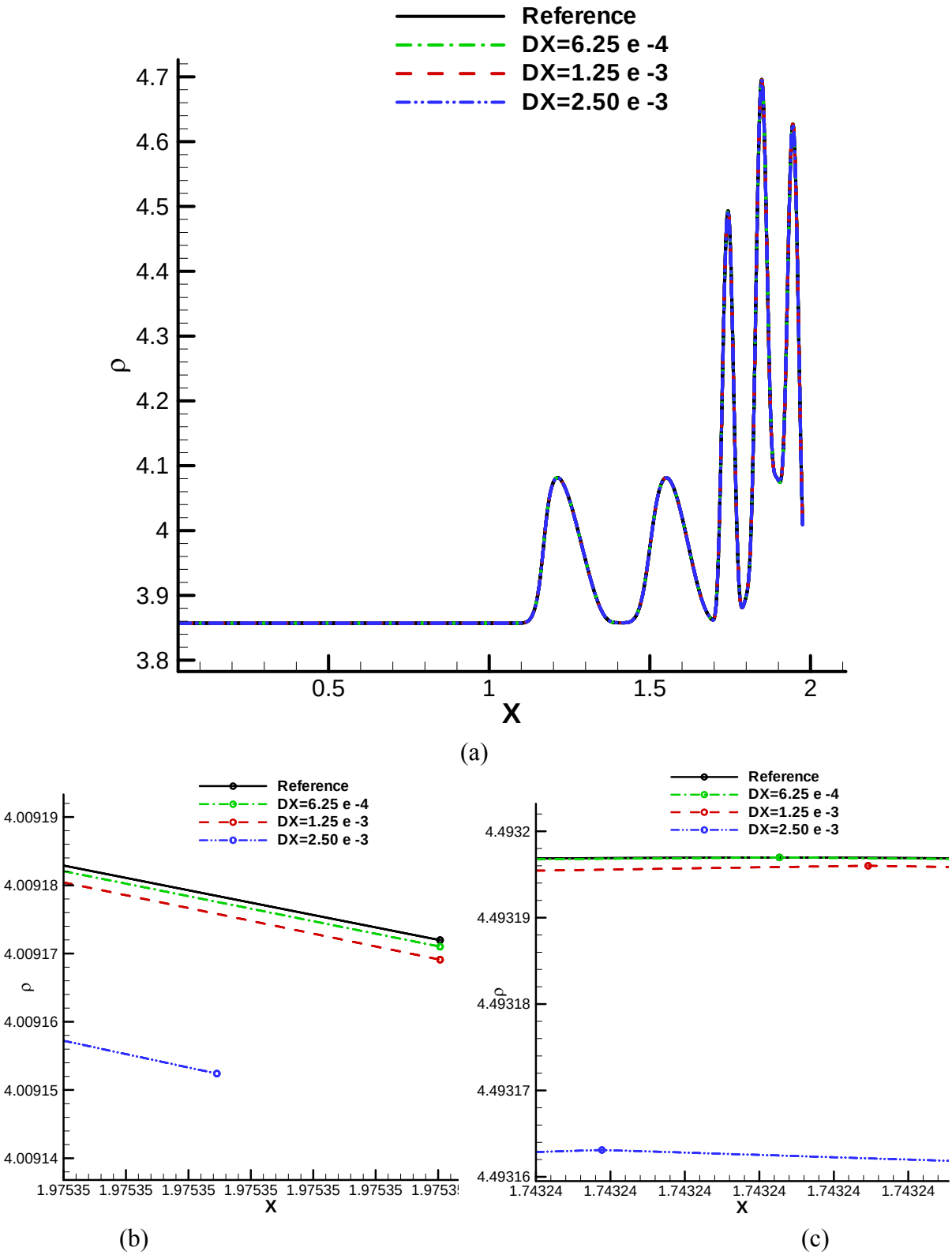

Fig.18: (a) Density variation for the smoother version of the Shu-Osher problem while using alternative shock acceleration method Eq.(40) for different grid sets. (b) and (c) are zoomed versions of the profile showing convergence.

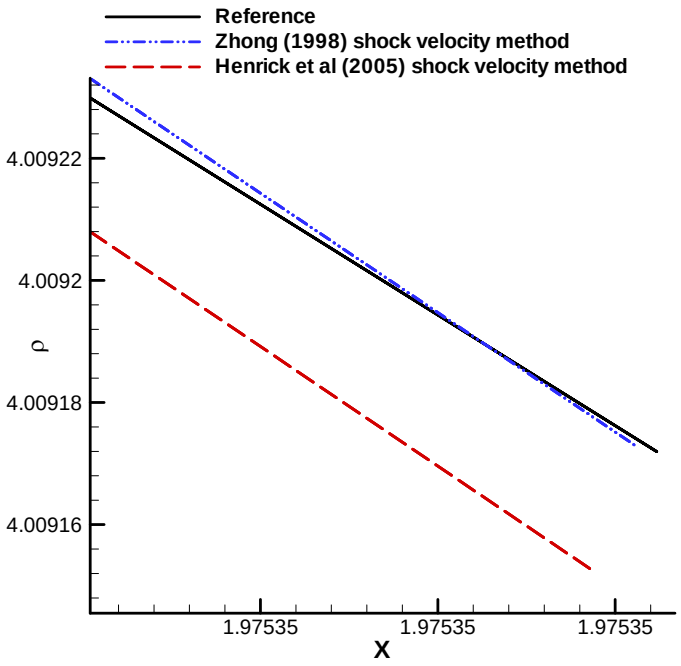

(a)

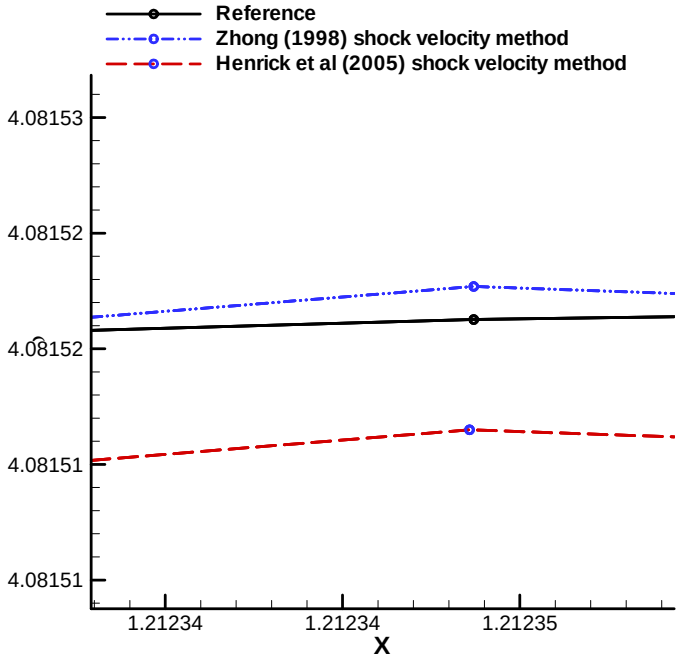

(b)

Fig.19: Comparison of density variation obtained from alternative shock-acceleration method with that obtained from Zhong's shock acceleration method and reference values (a) and (b) represent zoomed portions near and away from the shock respectively. ($dx = 2.5e-3$)

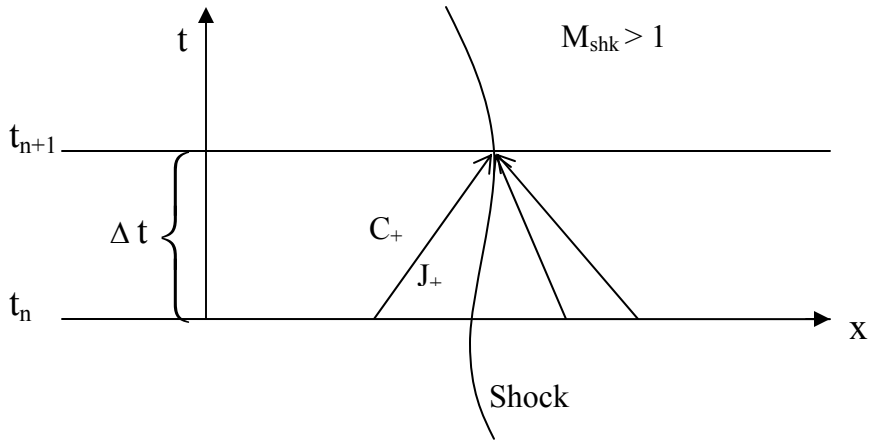

Fig. 20: Finding shock velocity based on value of Riemann invariant from behind the shock (J_+).

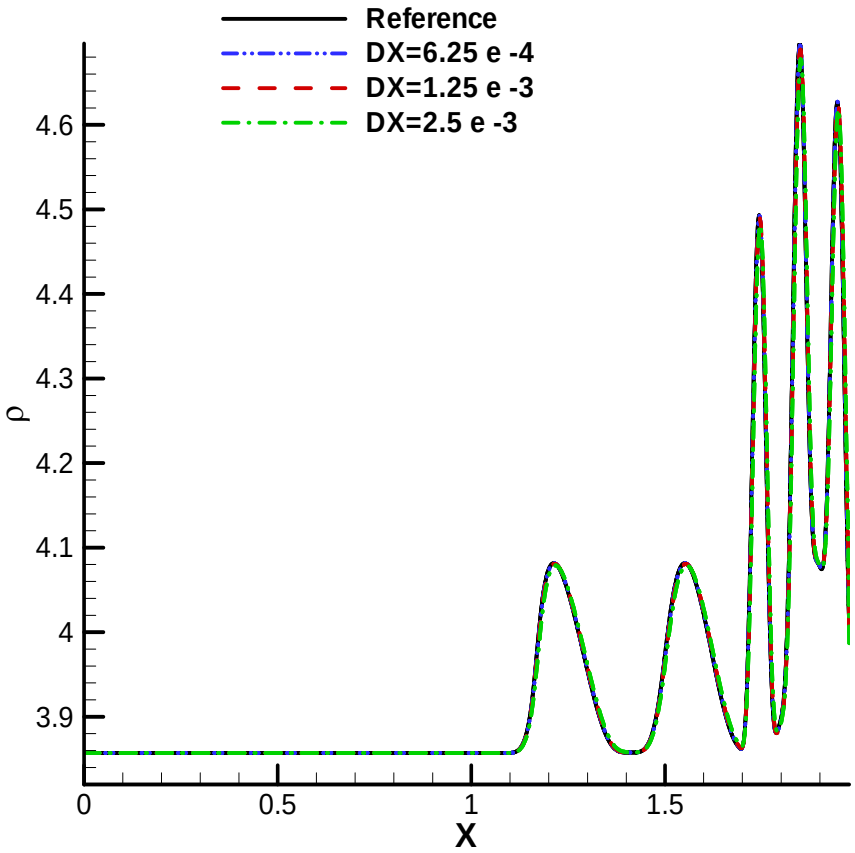

(a)

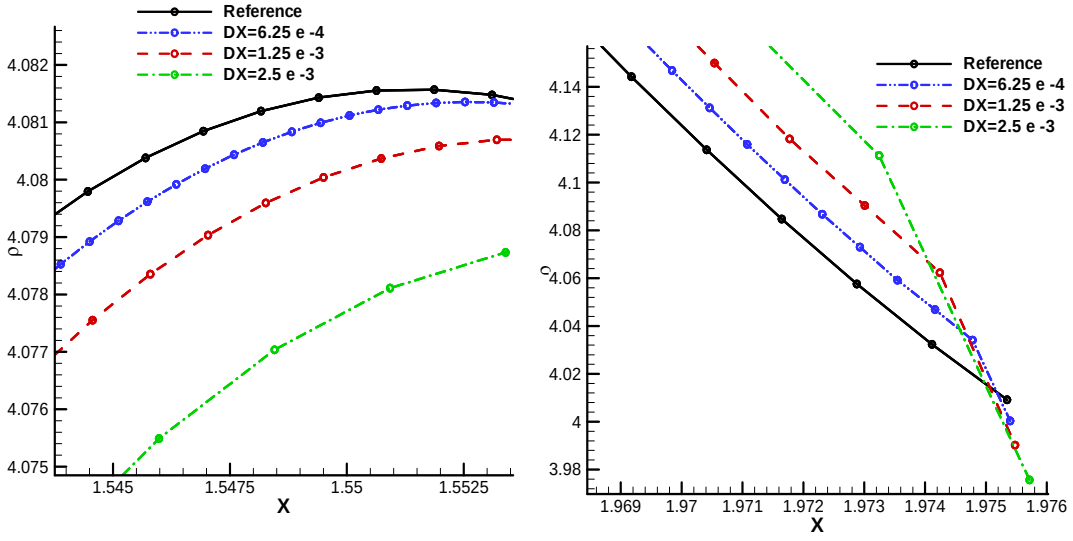

(b) (c)

Fig. 21: (a) Density variation for the smoother version of the Shu-Osher problem for different grid sets using Riemann invariants to find the shock-velocity. (b) and (c) are zoomed versions of the profile showing convergence.

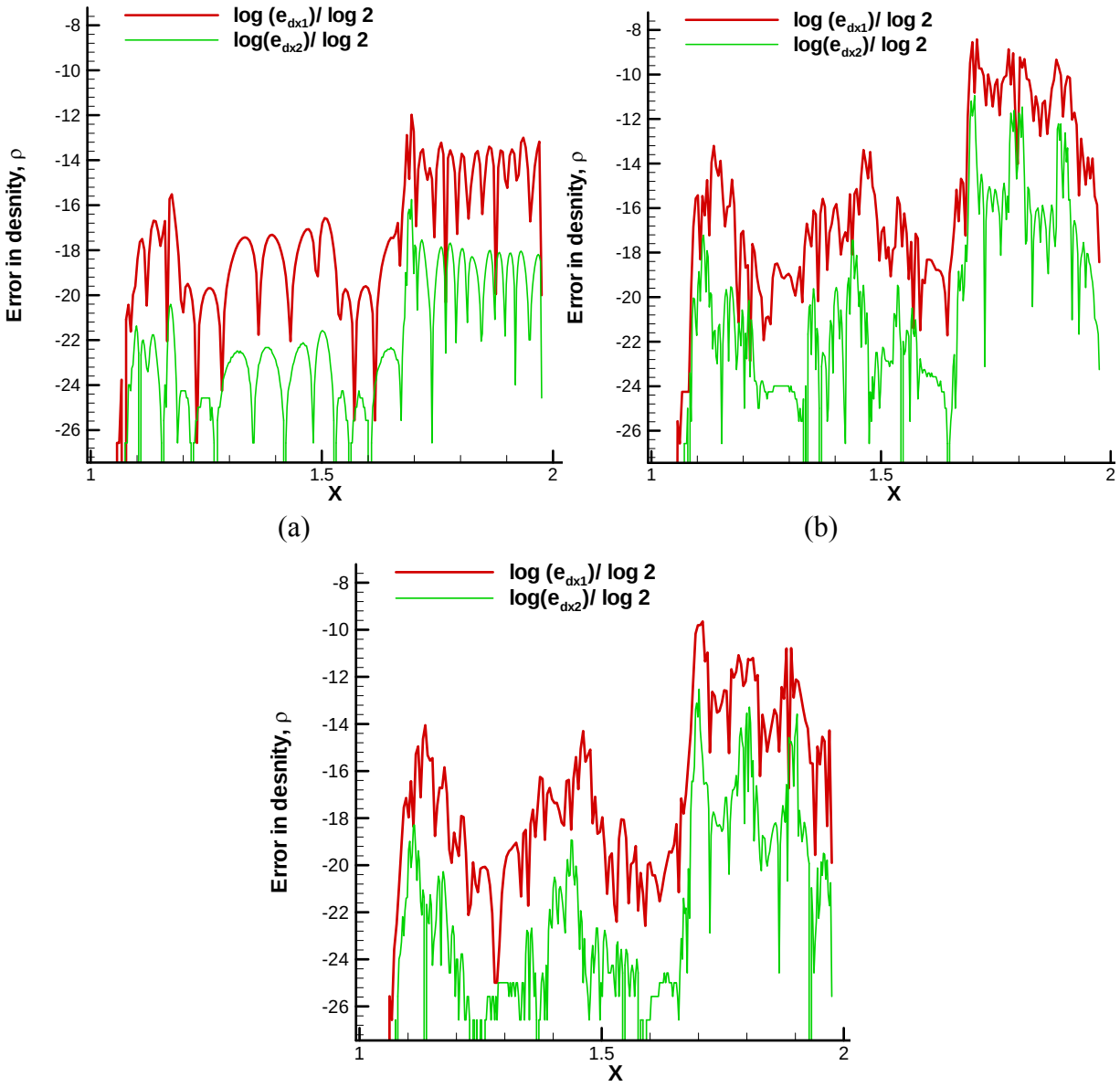

Fig. 22: Comparison of point-wise errors, e_{dx1} and e_{dx2} in density values solved by shock-fitting combined with (a) upwind central difference scheme (b) WENO5 scheme (c) mapped WENO5M scheme for smoother Shu-Osher problem.

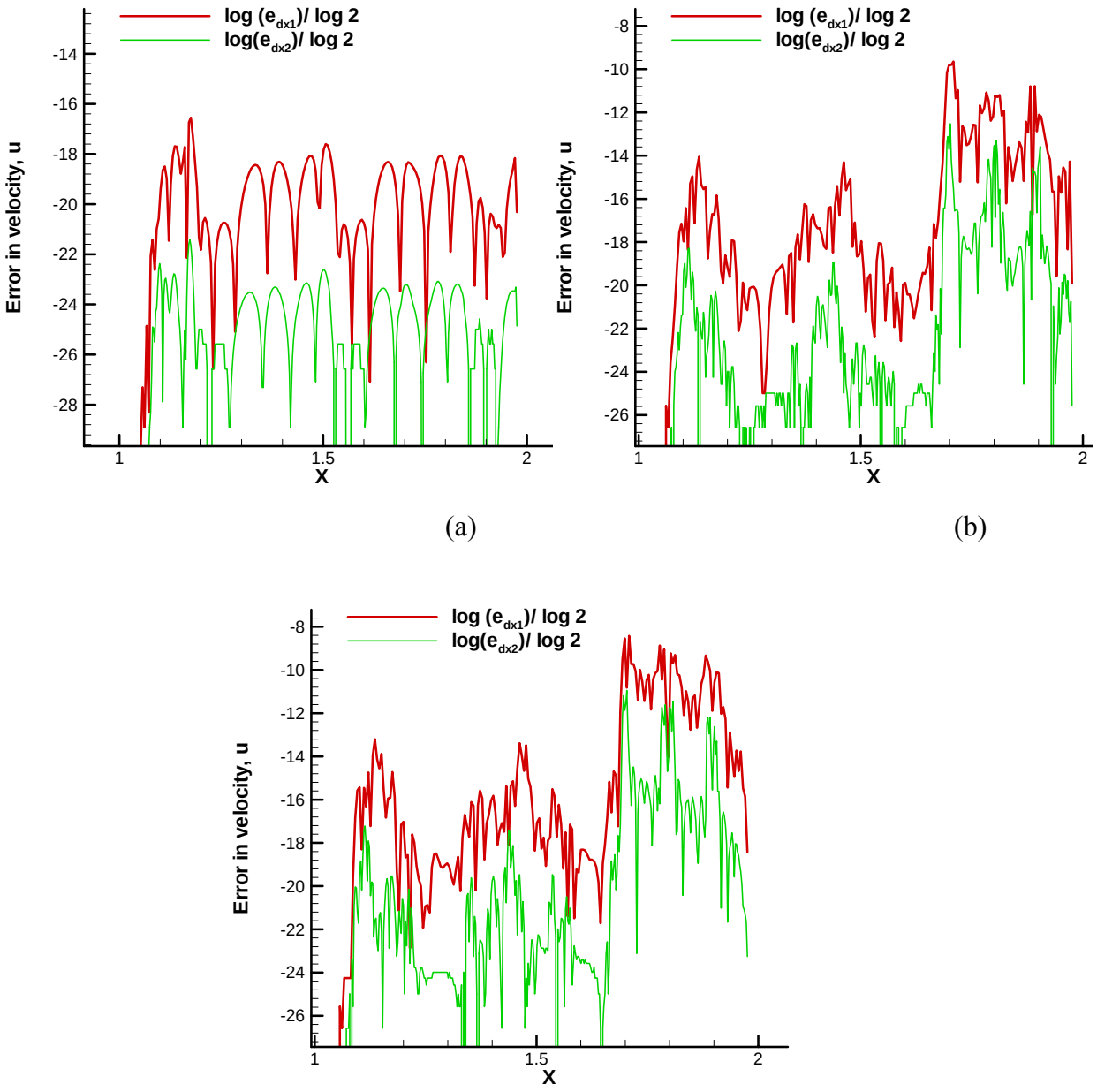

Fig. 23: Comparison of point-wise errors, e_{dx1} and in velocity values solved by shock-fitting combined with (a) upwind finite difference scheme (b) WENO5 scheme (c) mapped WENO5 scheme for smoother Shu-Osher problem.

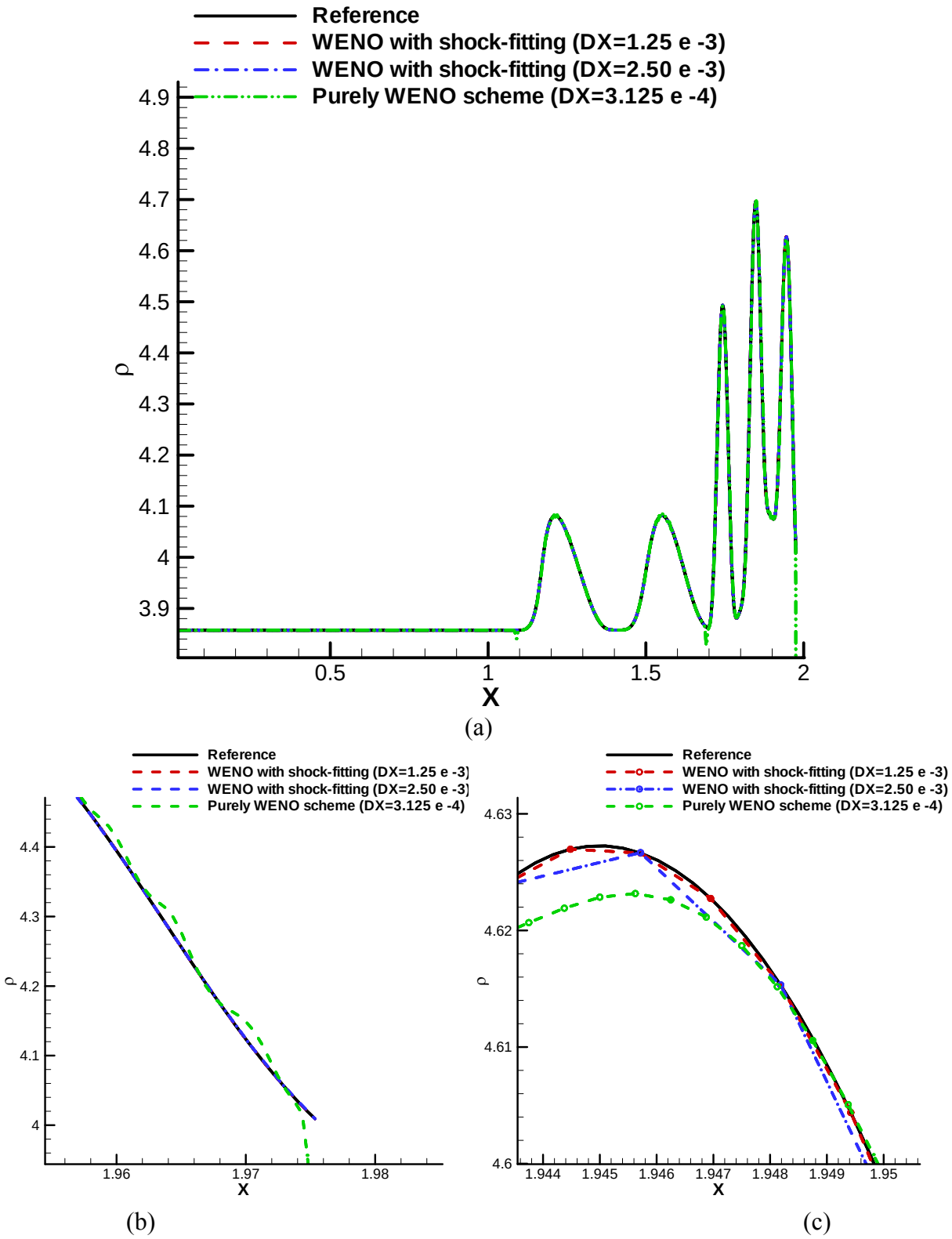

Fig. 24: (a) Comparison of density variation obtained from WENO scheme with and without fitting the shock . (b) and (c) are zoomed versions of the profiles.

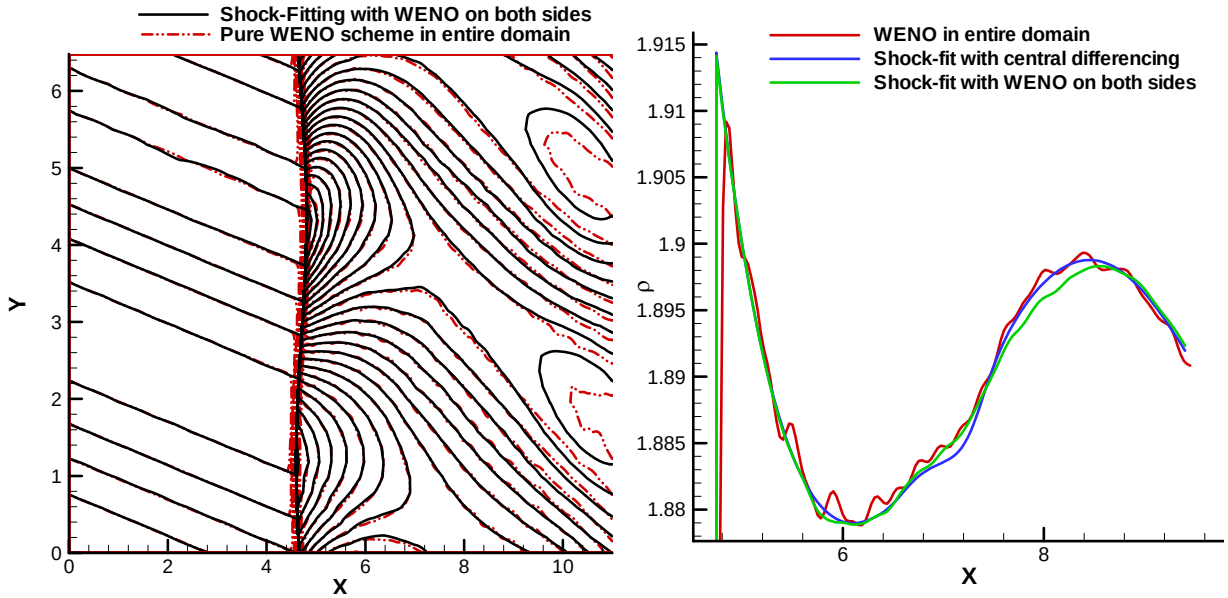

Fig. 25: (a) comparison of density contours obtained from WENO5 scheme at $t = 10\ s$ with and without shock-fitting methodology and (c) variation of density along $y = \pi$ line.